GAPDH Overexpression in the T Cell Lineage Promotes Angioimmunoblastic T Cell Lymphoma through an NF-κB-Dependent Mechanism

Laura Mondragón, Rana Mhaidly, Gian Marco de Donatis, Marie Tosolini, Pascal Dao, Anthony Martin, Caroline Pons, Johanna Chiche, Marie Jacquin, Véronique Imbert, et al.

GAPDH overexpression in the T cell lineage promotes angioimmunoblastic T cell lymphoma through an NF-κB dependent mechanism

Laura Mondragón[1,*], Rana Mhaidly[1,*], Gian Marco De Donatis[1], Marie Tosolini[2], Pascal Dao[3], Anthony R. Martin[3], Caroline Pons[1], Johanna Chiche[1], Marie Jacquin[1], Véronique Imbert[1], Emma Proïcs[1], Laurent Boyer[1], Anne Doye[1], Frédéric Luciano[1], Jaap G. Neels[1,] Frédéric Coutant[4,5], Nicole Fabien[4], Laura Sormani[1],Camila Rubio-Patiño[1], Jozef P. Bossowski[1], Florian Muller[1], Sandrine Marchetti[1], Elodie Villa[1], Jean-François Peyron[1], Philippe Gaulard[6], François Lemonnier[6], Vahid Asnafi[8], Laurent Genestier[9], Rachid Benhida[3], Jean-Jacques Fournié[10], Thierry Passeron[1,11], Jean-Ehrland Ricci[1,13,14] and Els Verhoeyen[1,12,13,14,15].

[1]Université Côte d'Azur, INSERM, C3M, 06204 Nice, France.
[2]Pôle Technologique du CRCT – Plateau Bioinformatique INSERM-UMR1037
[3]Institut de Chimie de Nice UMR UNS-CNRS 7272, Université Nice Sophia Antipolis, Parc Valrose, 06108 Nice, France
[4]Immunology Department, Lyon-Sud Hospital, Hospices Civils de Lyon, Pierre-Bénite, France
[5]Immunogenomics and Inflammation Research Unit EA 4130, University of Lyon, Edouard Herriot Hospital, Lyon, France
[6]Université Paris-Est Créteil; Institut Mondor de Recherche Biomédicale, INSERMU955; Département de Pathologie, Hôpitaux Universitaires Henri Mondor, Assistance publique des Hôpitaux de Paris, Créteil, France.
[7]Université Paris-Est Créteil; Institut Mondor de Recherche Biomédicale, INSERMU955; Unité hémopathies lymphoïdes, Hôpitaux Universitaires Henri Mondor, Assistance publique des Hôpitaux de Paris, Créteil, France
[8] Université Paris 5, Institut Necker-Enfants Malades (INEM), Institut national de recherche médicale (INSERM) U1151, and Laboratory of Onco-Hematology, Assistance Publique-Hôpitaux de Paris (AP-HP), Hôpital Necker Enfants-Malades, Paris, France
[9]CRCI ; INSERMU1052-CNRS UMR5286 ; Centre Léon Bérard ; Faculté de Médecine Lyon Sud, Université Claude Bernard Lyon I, 69921 Oullins Cedex, France.
[10]CRCT; INSERM U1037-Université Paul Sabatier-CNRS ERL5294, Université de Toulouse; Laboratoire d'Excellence TOUCAN; Programme Hospitalo-Universitaire en Cancérologie CAPTOR, Toulouse, France; IUCT, 31037 Toulouse, France
[11]Université Côte d'Azur. Centre Hospitalier Universitaire de Nice. Department of Dermatology. 06204 Nice, France
[12]CIRI, Université de Lyon; INSERM U1111; ENS de Lyon; Université Lyon1 ; CNRS, UMR 5308, 69007 Lyon, France
[13]Senior authors
[14]Correspondance: Els Verhoeyen (els.verhoeyen@unice.fr/els.verhoeyen@ens-lyon.fr) and Jean-Ehrland Ricci (ricci@unice.fr)
[15]Lead contact
[*]These authors have contributed equally

Summary

GAPDH is emerging as a key player in T cell development and function. To investigate the role of GAPDH in T cells, we generated a transgenic mouse model overexpressing GAPDH in the T cell lineage. Aged mice developed a peripheral Tfh-like lymphoma that recapitulated key molecular, pathological, and immunophenotypic features of human angioimmunoblastic T cell lymphoma (AITL). GAPDH induced non-canonical NF-κB pathway activation in mouse T cells, which was strongly activated in human AITL. We developed a NIK inhibitor to reveal that targeting the NF-κB pathway prolonged AITL-bearing mouse survival alone and in combination with anti-PD-1. These findings suggest the therapeutic potential of targeting NF-κB signaling in AITL and provide a model for future AITL therapeutic investigations.

Clinical significance

Availability of preclinical mouse models for rare cancers is a prerequisite for revealing important pathways and targets in order to identify and evaluate possible treatment regimens for these patients lacking treatment options. Our GAPDH transgenic mouse model developed a Tfh-like lymphoma with a strong germinal center B cell component, mimicking angioimmunoblastic T cell lymphoma (AITL), a rare aggressive lymphoma. Our data confirmed that GAPDH-induced AITL disease depends mechanistically on activation of the non-canonical NF-κB pathway, which we also confirmed to be activated in human AITL. Targeting this pathway with an NF-κB pathway inhibiting drug was an effective treatment for murine as well as human AITL cells. This mouse model allows testing of therapeutic options for AITL including immunotherapy.

Introduction

Immunometabolism has recently become an intense field of research. It shapes the functions and the differentiation of immune cells and reveals anti-cancer immunotherapies (Pearce and Pearce, 2018). Fundamental changes from mitochondrial to glycolytic metabolism are implemented by immune cells as well as cancer cells to meet their high energy requirement, (Warburg effect) (Galluzzi et al., 2013; Kroemer and Pouyssegur, 2008). However, the role of specific metabolic enzymes in T cells and cancer is just starting to be unraveled. Aerobic glycolysis converts glucose to pyruvate through a series of 10 enzymes, of which one is of particular interest: the glyceraldehyde-3-phosphate dehydrogenase (GAPDH). Recent studies have demonstrated that GAPDH could have a rate-limiting function in the context of Warburg effects (Liberti et al., 2017). In addition to its role in glycolysis, GAPDH is a multifunctional protein with numerous non-glycolytic functions (Colell et al., 2009; Colell et al., 2007; Jacquin et al., 2013; Lavallard et al., 2009). GAPDH is overexpressed in many cancers (Chiche et al., 2015; Liberti et al., 2017; Revillion et al., 2000), but is role in tumorigenesis is still unclear (Revillion et al., 2000). Moreover, we previously revealed GAPDH overexpression in chronic myeloid leukemia (CML) cells, which participated in CML resistance to chemotherapeutic treatment (Lavallard et al., 2009). Of note, overexpression of GAPDH, but not other glycolytic enzymes tested, protected cells from caspase-independent cell death (CICD) through persistence of a few intact mitochondria that might facilitate tumor cell survival and chemotherapy resistance (Colell et al., 2007).

To date, very little is known about GAPDH expression levels and its role in T cell differentiation and T cell cancers such as peripheral T cell lymphomas (PTCL) but GAPDH has recently emergd as a key factor in T cell survival, activation and function (Balmer et al., 2016; Chang et al., 2013; Xu et al., 2016). For example, GAPDH expression was implicated in T cell responses under hypoxia (Dimeloe et al., 2016; Xu et al., 2016). Acetylation of GAPDH enhances its activity, boosting rapid memory $CD8^+$ T cell responses (Balmer et al., 2016). Interestingly, GAPDH can also modulate T cell effector function (Chang et al., 2013). We and others established a clear connection between high GAPDH expression and the activation of the NF-κB pathway (Chiche et al., 2015; Gao et al., 2013). We recently showed that elevated GAPDH expression was found to promote NF-κB activation in a non-Hodgkin's B cell lymphoma via binding to tumor necrosis factor receptor-associated factor-2 (TRAF2), which enhanced the transcription and the activity of HIF-1α (Chiche et al., 2015). NF-κB activation occurs via two major signaling pathways. The canonical pathway mediates the

activation of NF-κB1 p50, RelA and c-Rel, whereas the non-canonical NF-κB pathway selectively activates p100-sequestered NF-κB members, predominantly NF-κB p52 and RelB. The canonical NF-κB pathway responds to engagement of immune-receptors and results in rapid but transient NF-κB activation (Sun, 2017). In contrast, activation of the non-canonical pathway is characteristically slow and persistent and ligands of the TNFR superfamily are inducers of the non-canonical pathway. Both NF-κB pathways are involved in malignancy and inflammatory diseases (Cildir et al., 2016; Hoesel and Schmid, 2013; Sun, 2017). Importantly, NF-κB activation is associated with many T cell cancers (Balmer et al., 2016; Cildir et al., 2016; Gerondakis et al., 2014; Imbert and Peyron, 2017; Sun, 2017) and plays an essential role in T-cell development and function (Gerondakis et al., 2014; Grinberg-Bleyer et al., 2017; Long et al., 2009). It is for example implicated in differentiation and function of regulatory T cell (Grinberg-Bleyer et al., 2017; Long et al., 2009; Vasanthakumar et al., 2017) (Jimi et al., 2008). However, the contribution of GAPDH to T cell function, differentiation and possibly T cell malignancy remains to be comprehensively elucidated

Results

Overexpression of GAPDH exclusively in the T cell lineage does not affect early T cell differentiation

To uncover GAPDH function in T cells, we generated a transgenic mouse model, in which GAPDH was overexpressed under the control of the T cell specific promoter, plck. A V5-tag was fused to GAPDH to distinguish it from the endogenous GAPDH enzyme, and 3 founder animals (F16, F07 and F35) were identified (Figure 1A). Overexpression of GAPDH was validated in the plck-GAPDH transgenic mice by western blot (Figure 1B). We confirmed exclusive and strong expression in the T cell lineage (Figure 1C). GADPH-V5 was significantly overexpressed in different thymic subpopulations of the founder plck-GAPDH mice at 4-weeks of age compared to WT (Figure 1D). Higher overall GAPDH expression was detected in F07 and F35 thymocytes than in F16 thymocytes (Figure 1E). Notably, although GAPDH was described to inhibit a non-apoptotic cell death named CICD (Colell et al., 2007), which might play a role in thymocyte development and selection, no significant differences in thymic subpopulations were revealed in 4-week old mice (Figure 1F).

Aged plck-GAPDH mice develop a peripheral T cell lymphoma-like pathology

Upon aging, the plck-GAPDH mice developed tumors (Figure 2A). Tumor frequency coincided with the GAPDH overexpression levels (Figure 1D and 2A), as the high GAPDH expressing F07 and F35 mice all developed tumors, while tumor frequency for F16 was much lower and with delayed onset of disease (Figure 2A and data not shown). Therefore, we focused our study on F07 and F35. These plck-GAPDH mice showed onset of disease at 18 months or older (Figure 2B). Aged plck-GAPDH mice developed a pathology characterized by a generalized lymphadenopathy (Figure 2C). These mice generally developed splenomegaly and frequently developed hepatomegaly and enlarged mesenchymal lymph nodes (MES LN) and LNs at ectopic sites such as around the kidney, heart or intestines (Figures 2D-2G). The spleens and LNs showed a greatly altered architecture, and the follicular structures visible in the WT were destroyed in the plck-GAPDH mice, marked by large polymorphic infiltration of T cells and B cells (Figures 2H and S1A). These pathological features pointed towards a peripheral T cell lymphoma (PTCL). Remarkably, aged plck-GAPDH mice also developed a typical skin rash and showed a strong LN vascularization with detection of 35-fold increased VEGF expression level in mPTCL LN vs WT and the presence of venules ($CD31^+$) in the LN (Figure S1B-D). Moreover, 50% of plck-GAPDH mice developed ascites in the abdominal region (data not shown). Finally, the splenic tumors of the transgenic mice were characterized by no changes in $CD19^+$ B cell counts but a 2-fold higher cellularity of T cells and an increased ratio of $CD4^+$ to $CD8^+$ T cells (Figures 2I and 2J). The combination of all these histopathological symptoms suggests that the plck-GAPDH mice developed a PTCL.

Plck-GAPDH mice develop a T cell lymphoma with a T follicular helper dominance.

Since tumors in plck-GAPDH mice manifested a higher presence of $CD4^+$ over $CD8^+$ T cells, we characterized the $CD4^+$ T cells. They were positive for programmed cell death 1 (PD-1) and to a lesser extent for the chemokine receptor, CXCR5 (Figure 3A). The percentage of $CD4^+PD\text{-}1^{high}CXCR5^+$ T follicular helper (Tfh)-like cells was significantly higher in plck-GAPDH than in WT spleens and the increase in total $CD4^+PD\text{-}1^{high}$ was even more pronounced (80%; Figure 3B).

Additionally, two Tfh markers, ICOS (Hu et al., 2011) and Bcl-6, were upregulated on the tumor $CD4^+$ T cells (Figure 3A). They also had an activated memory phenotype (Figure 3C) and showed increased expression of the death receptor FAS (CD95) but only slight

augmentation of FAS ligand (FASL, CD178) compared to $CD4^+$ WT T cells (Figure 3D), both characteristics of Tfh cells. Ki67 staining indicated that these $CD4^+$ T splenocytes were strongly cycling in contrast to WT splenocytes (Figure 3E), indicating the aggressiveness of these malignant T cells. When we activated $CD4^+$ plck-GAPDH tumor cells by PMA/ionomycin, a strong expression of the inflammatory cytokines (TNFα and IFNγ) and the anti-inflammatory cytokine IL-10 was revealed (Figure 3F). IL-10 is known to promote B cell expansion. In contrast, IL-4 (Th2 marker) and IL-17 (Th17 marker) expression was not increased (data not shown). Finally, we clearly detected a TCRβ and TCRγ receptor oligoclonality in the $CD4^+$ T cells from different plck-GAPDH tumor bearing mice (Figures 3G and 3H).

The above results together indicate the plck-GAPDH mice developed a PTCL with a pronounced Tfh-like phenotype.

Plck-GAPDH Tfh-like lymphoma is associated with germinal center and plasma B cells

Tfh reside in germinal centers (GCs) and normally interact with GC B cells, ultimately yielding plasma cells (PCs) and memory B cells (Cildir et al., 2016). Indeed, B cell phenotyping of cells in the enlarged spleens and LNs of the plck-GAPDH mice demonstrated significantly increased percentages of $CD95^+GL\text{-}7^+$ GC B cells compared to WT (Figures 4A and 4B). Additionally, plck-GADPH B cells demonstrated increased levels of FAS and FASL compared to WT (Figure 4C) underlining the importance of Tfh FAS and GC B FASL interaction for cell survival. PD-1 expression on Tfh not only regulates GC survival but also impacts plasma cell (PC) differentiation (Hu et al., 2011; Xu et al., 2014). Identification of PCs by $CD138^+CD19^-B220^{low}$ surface expression showed that 60% of the plck-GAPDH tumor mice showed more PCs than WT mice (PC WT < 5%) varying from 6 to 80% of total mononuclear cells (Figure 4D and 4E).

Co-residence of Tfh, GC and plasma B cells in the plck-GAPDH tumors stresses that this mouse model closely mimics a human Tfh PTCL cancer (Ahsanuddin et al., 2011; Nagoshi et al., 2013). We also detected cycling B cells, hypergammaglobulinemia and presence of autoantibodies in the sera of mPTCL bearing plck-GAPDH (Figure S2A-C). This notion of a PTLC is further reinforced by increased numbers of tumor-associated myeloid cells, specifically follicular dendritic cells (FDCs) ($CD35^+$) and total DCs ($CD11c^+$), in the enlarged plck-GAPDH LNs compared to WT mice (Figures S1C and S2D). Of note, strong infiltration

of the $CD4^+PD\text{-}1^+$ Tfh cells and GC B cells in the bone marrow was confirmed in all tumor bearing plck-GAPDH mice (Figure S2E).

To confirm that the plck-GAPDH mouse developed a rare T cell lymphoma we transferred the tumor cells from enlarged LN or spleens into NOD/SCID $\gamma c^{-/-}$(NSG) recipient mice (Traggiai et al., 2004). Engrafted NSG mice recapitulated the disease characteristics of the plck-GAPDH donor mice (Figure S2F). Tumors showed a strong increase of $CD4^+/CD8^+$ T cell ratio (Figure S2G), high expression of PD-1 on $CD4^+$ T cells, and the co-residence of GC B cells in the tumors (Figure 4F). We confirmed Tfh and GC B cell colonization of the spleen in 3 independent NSG recipients per donor (Figure 4G). We also detected infiltration of Tfh and GC B cells in the BM of recipient NSG mice (Figure S2H) and confirmed that engrafted T cells conserved oligoclonality for the TCRβ chain (Figure S2I).

Co-residence of Tfh, GC and plasma B cells and tumor associated cells in the plck-GAPDH tumors stresses that this mouse model strongly mimics a human Tfh PTCL.

Plck-GAPDH PTCLs have a gene expression profile resembling that of AITL patient PTCL

To identify the human PTCL (hPTCL) counterpart of the PTCL developed by plck-GAPDH mice (mPTCL), we compared the gene expression profile (GEP) of our mPTCL to those of hPTCLs. The mPTCLs contained on average 30.0±6.2% $CD4^+$ cells. Initially, we compared GEPs of murine splenic PTCLs and normal WT splenocytes, identifying 471 up- and 847 down-regulated genes. Gene set enrichment analysis (GSEA) for a Tfh-upregulated gene set (18 genes), based on previous studies (de Leval et al., 2007; Jain et al., 2015), showed upregulation of Tfh signature genes and signature enrichment in the murine lymphomas as compared to WT (Figure 5A and 5B). This was already suggested by their immuno-phenotype ($CD4^+CXCR5^+ICOS^+PD\text{-}1^{high}$, Figure 3A-E). To further validate the Tfh characteristics, we confirmed the upregulated expression of CXCL13, IL-21 and Bcl-6, all Tfh regulators, in mPTCL isolated $CD4^+$ T cells as compared to WT $CD4^+$ splenocytes (Figure 5C). In contrast, BLIMP, an antagonist regulator of Tfh cell differentiation was not upregulated (Johnston et al., 2009).

Additionally, GSEA for a GC-plasma B cell signature (24 genes) (Recaldin and Fear, 2016) showed an upregulation of GC- and PC-enriched gene expression in mPTCLs (Figure 5D and 5E), indicating that we have a mixed GC and PC B-cell signature.

One of most prominent hPTCL with Tfh dominance associated with GC/plasma B cells is angioimmunoblastic T cell lymphoma (AITL), a rare devastating cancer (Federico et al.,

2013). The described pathological and immunophenotypic characteristics of the plck-GAPDH mPTCL closely matches human AITL (hAITL) (Table S1). Indeed, when we compared the GEP data of LNs from 60 AITL patients to healthy LN, we found increased expression of CXCR5, PD-1, CXCL13, Bcl-6, ICOS and IL-21 confirming the Tfh neoplastic expression pattern in the analyzed AITL patient cohorts (de Leval et al., 2007; Iqbal et al., 2014; Roth et al., 2006), similar to the plck-GAPDH mPTCLs (Figure S3A). The GC and PC B cell signature in the AITL patients (Figure S3B) also matched the plck-GAPDH mPTCL. Finally, an even more specific AITL gene signature was confirmed in the mPTLCs (Figure S3C and S3D).

To further validate the AITL pathology, we decided to compare the cytokine and chemokine mRNA expression profiles of plck-GAPDH mouse LNs (Figure S3E) to AITL patient LNs. AITL is characterized by strong autoimmune features inflammatory signals (de Leval et al., 2007) such as increased IFNγ, IL1Rα, IL-6 and TNFα (Figure S3F). We confirmed the the mRNA expression data in figure S3E by quantification of secreted cytokines and chemokines in PMA/ionomycin stimulated plck-GAPDH mPTCL cells (Figure S3G). Increased levels of inflammatory (IFNγ, IL1Rα, IL-6 and TNFα) and anti-inflammatory cytokines (IL-10, IL-6) were comparable to an AITL gene enriched inflammation signature (Figure S3F and S3G). In AITL, Tfh and GC B cell and micoenvironment interaction is based on cytokine-chemokine cross-talks (Mourad et al., 2008). GEP of mPTCL *vs* WT splenocytes revealed an upregulated expression of multiple cytokines but also of chemokines corresponding to those of AITL patient LN (Figure S3H and S3I, Figure S3J and S3K). Moreover, our mPTCL clearly showed a prominent upregulation of humoral immune response genes (Table S2) confirming the presence of PCs in our tumors and vascularization in the LNs was confirmed by upregulation of vascularization related genes (Table S2). All these data confirmed again the match between mPTCL and AITL characteristic features (de Leval et al., 2010; de Leval et al., 2007). Interestingly, 1-year old premalignant plck-GAPDH mice showed no prominent skewing in the T and B cell populations (Figure S4A-D) except for the fact that a population of Tfh-like $CD4^+$ $PD\text{-}1^{high}$ T cells and GC B cells were starting to emerge (Figure S4E and S4F). However, no increased cytokine secretion, TCR-signaling, T cell activation, nor increased proliferation were detected in plck-GAPDH versus WT $CD4^+$ T cells from 1-year old mice (Figure S4G-J).

We confirmed that the glycolytic enzyme GAPDH was still strongly overexpressed in the mPTCLs at the mRNA and protein level compared to age-matched WT animals (Figure 5F). Strikingly, GAPDH expression was higher in AITL patient than healthy LNs (Figure 5G).

Metabolic pathway analysis did not show pronounced upregulation of glycolysis in the plck-GAPDH lymphoma (Figure 5H). In contrast, $CD4^+$ splenocytes from pre-malignant 1-year old plck-GAPDH mice showed upregulated glycolysis compared to WT, especially when activated through the TCR as detected by increased extracellular acidification rate (ECAR), glucose uptake and lactate production (Figure S4K, S4L and S4M). In plck-GAPDH mPTCL, we detected increased mitochondrial respiration (Figure 5H), which was already observed in $CD4^+$ T cells from 1-year old plck-GAPDH upon TCR engagement (Figure S4N).

AITL frequently carries a G17V (p.Gly17Val) mutation in *RHOA* (Palomero et al., 2014; Sakata-Yanagimoto et al., 2014), which encodes the small GTPase RHOA. In plck-GAPDH $CD4^+$ T cells isolated from tumors, we found two mutations in the effector domain of *RHOA,* one point mutation at position 37 (T37M) present in all 15 plck-GAPDH tumors and an INDEL frameshift mutation consisting of a 5 bp insertion into codon 44 present in 4/15 plck-GAPDH tumors (Figure 6A). Sanger and whole exome sequencing of the WT C57BL6JOlaHsd strain used to generate the plck-GAPDH mice indicated that the T37M mutation and INDEL were not present in the germline (Figures S5A and S5B). The point mutation T37M reduced RHOA activity as measured by the reduced affinity for the GST-rhotekin RBD compared to the WT or the Q63L active mutant of RHOA (Figure 6B), identifying T37M as an inactivating mutation in RhoA. Additionally, the effect of the T37M mutation on RHOA was equivalent to the T37A mutation found in follicular lymphoma and gastric cancer (Figures 6B and 6C), and the activity of RHOA T37M was even lower than that for a well-established mutation (T19N) in the GTP/GDP binding domain (Figure 6B). The INDEL frameshift mutation in *RHOA* is a truncating mutation, which would likely result in a truncated protein (Figure S5C).

Whole exome sequencing revealed additional mutations in the plck-GAPDH lymphoma $CD4^+$ cells (Tables S3-S6). Of note though, many of the identified mutations in epigenetic modifiers and TCR–signaling genes that were also mutated in hAITL were intronic or intergenic in our mPTCL and likely would not lead to loss of function (Tables S3 and S4).

The above data support that our mPTCL resembles in great detail hAITL indicating that the plck-GAPDH mouse model represents a valid model for this lymphoma.

Plck-GAPDH develop an AITL-like PTCL via a GAPDH-dependent activation of the NF-κB pathway.

Constitutive activation of the NF-κB signaling has been observed in various tumors including lymphomas and leukemia (Imbert and Peyron, 2017) and we have shown that GAPDH

enhances B lymphoma aggressiveness via activation of NF-κB (Chiche et al., 2015). Moreover, our GEP data showed that many NF-κB targets are upregulated in our plck-GAPDH tumors such as IFNγ, ICOS, IL-6, CCL5, CCL2, CCL4, CXCL9, 10 and 11, IgG heavy chains, CD40, CD44, ICAM-1 and IRF4. We confirmed an upregulation of the NF-κB canonical pathway target genes in thymocytes from 4-week old plck-GAPDH mice (Figure S6A). Activation of the canonical pathway was established by phosphorylation of p65 (Figure S6B) and the binding of TRAF2 to GAPDH (Figure S6C).

GSEA for a NF-κB gene signature (Gerondakis et al., 2014) showed upregulation of the NF-κB canonical and non-canonical pathway as well as of their target genes in the plck-GAPDH mPTCL compared to WT splenocytes (Figures 7A and 7B), which was confirmed by q-PCR analysis of isolated $CD4^+$-cells from mPTCL (Figures 7C and 7D). Activation of the non-canonical pathway was confirmed by increased phosphorylation of p100 and its cleavage into p52 in $CD4^+$ mPTCL cells as compared to WT splenocytes (Figure S6D).

We also detected in hAITL a slight upregultation of the canonical NF-κB pathway (Figure 7E) and a strong activation of the non-canonical NF-κB pathway (Figure 7F) characterized by increased RelB expression and strong upregulation of the non-canonical target genes EZH2 and IRF4, while other non-canonical targets, SP-1 and ENPP2, were not or slightly upregulated, equivalent to the mPTCL (Figure 7E and 7F).

Finally, to establish whether the modulation of NF-κB pathway is a central event in mPTCL induction, we aged plck-$p65^{-/-}$ mice, unable to activate the canonical NF-κB pathway in T cells, and plck-$I\kappa B^{-/-}$ mice, characterized by a constitutive activation of the NF-κB pathway in the T cell compartment. At 18 months, the plck-$I\kappa B^{-/-}$ mice developed a Tfh T cell lymphoma with $CXCR5^+PD\text{-}1^+CD4^+$ T cells and $CD95^+GL\text{-}7^+$ GC B cells, an increased $CD4^+/CD8^+$ T cell ratio and higher GAPDH, IL-21, CXCL13, and Bcl-6 expression levels (Figures 7G and 7H). Also upregulation of the non-canonical NF-κB pathway was detected in $CD4^+$ cells from the plck-$I\kappa B^{-/-}$ mPTCL (Figure S6E). All these features are identical to mPTCL developed by plck-GAPDH mice. Additionally, $CD4^+$ splenocytes from 1-year old pre-malignant plck-GAPDH mice had upregulated the canonical NF-κB pathway and initiated the upregulation of the non-canonical pathway (Figure S6F). To further confirm the role of GAPDH in NF-κB activation, we generated plck-GAPDH/$p65^{-/-}$, in which the canonical NF-κB pathway is inactivated. Since the development of plck-GAPDH tumors can take over 2 years, we isolated splenic $CD4^+$ cells from age-matched WT, plck-GAPDH, plck-$p65^{-/-}$ and plck-GAPDH/$p65^{-/-}$ mice and cultured them under Tfh inducing conditions. Only the plck-GAPDH derived $CD4^+$

cells expressed Tfh markers at 3 weeks of culture (Figure S6G), accompanied by upregulation of the canonical and non-canonical NF-κB pathway (Figure S6H), while plck-GAPDH/p65$^{-/-}$ CD4^{+} T cells were equivalent to WT. This underlined the importance of induction of the NF-κB pathway by GAPDH in accelerated Tfh development.

Finally, we evaluated if GAPDH is still required for mPTCL growth once established. Ten NSG mice were engrafted with plck-GAPDH lymphoma and were treated upon tumor establishment with a GAPDH specific inhibitor, koningic acid (KA), or vehicle (Figure S6I). No difference in survival of the 2 groups of mice was detected (Figure S6J). Despite a reduction in GAPDH activity in the KA-treated mice (Figure S6K), both groups developed splenomegaly (Figure S6L), and the KA-treated group did not show a change in B, T or Tfh CD4^{+}PD-1^{high} cells nor in NF-κB activity (Figures S6M-P). This suggests that, while GAPDH can drive mPTCL development, it is not required to maintain mPTCL tumor growth once it is established.

This indicates that GAPDH-induced constitutive activation of the NF-κB pathway in T cells results in a dominant Tfh PTCL equivalent to AITL, underlined by a shift towards the NF-κB non-canonical pathway in the tumor cells.

Plck-GAPDH mouse developing AITL respond to non-canonical NF-κB inhibition and anti-PD-1 treatment

Activation of the non-canonical pathway depends on the activation of the NF-κB inducing kinase (NIK) and IKKα phosphorylation (Xiao et al., 2001). We confirmed a 9-fold and 3-fold increased NIK expression in the mPTCL CD4^{+} T cells and CD19^{+} GC B cells compared to WT counterparts, respectively (Figure 8A), suggesting NIK could represent a therapeutic target in AITL. PD-1 and its ligand PD-L1, which play a central role in down-modulation of anti-tumor immunity (Topalian et al., 2016) might also represent AITL therapeutic targets. High PD-1 expression was characteristic for CD4^{+} Tfh cells in our plck-GAPDH AITL-like tumors (Figure 3A and B). Therefore, we opted to investigate treatments with a NIK inhibitor alone or in combination with anti-PD-1 in our AITL model.

Due to a lack of specific NIK inhibitors, we developed NIK^{inh}, a substituted halo-quinoline derivative characterized by potent anti-NIK activity (patent PCT/EP2017/067306; Figure S7A). NIK^{inh} was able to inhibit NIK's ability to phosphorylate a substrate protein *in vitro* in an ATP dependent manner (ADP-Glo assay; Figure S7A), demonstrating inhibition of NIK ATPase activity. Using a biotinylated version of the drug (NIK^{inh}-biotin) compared to biotin

alone or mock conjugated biotin (phenyl-biotin and aminoquinolinyl-biotin), we confirmed that NIK^{inh}-biotin was able to affinity precipitate NIK (Figure S7B). Increasing the ratio of free NIK^{inh} and NIK^{inh}-biotin (1:1 and 10:1) reduced the amount of NIK precipitated (Figure S7B), which indicates the observed interaction between the NIK^{inh} and NIK is specific. NIK^{inh} also reduced EZH2 expression, a downstream target of NIK, in a dose-dependent manner in a melanoma cell line characterized by upregulation of non-canonical pathway (A375), and it concomitantly increased the expression of CDKN1A/p21 (Figure S7C). Additionally, we showed that this NIK^{inh} decreased cleavage of p100 into p52, and EZH2 at the protein level in A375 cells, lung cancer cells (A549), and freshly isolated patient melanoma cells (C12.06)(Figure S7D). We then compared the effects of our NIK^{inh} with those of NF-κB2-siRNA on the proliferation of the A375, C12.06, and A549 cancer cells. The treatments had similar inhibitory effects on the proliferation of the cancer cells and no effect on normal human melanocytes or fibroblasts (Figure S7E), emphasizing that the inhibitor is specific for cancer cells that have the non-canonical NF-κB pathway upregulated. Moreover, we have confirmed these data also in 3 different diffuse large B cell lymphoma cell lines (U2932, Karpas 422, SUDHL-6; Figure S7F).

We next evaluated treatment with this NIK^{inh} alone or in combination with an anti-PD-1 *in vivo* in our AITL transplant model. Both NIK^{inh} single treatment or combined with anti-PD-1 resulted in significantly increased survival of up to 60% and 70% of the plck-GAPDH tumor engrafted mice, respectively, compared to control-treated mice (Figure 8B). At sacrifice, we detected a significant decrease in spleen size for the single and double treated mice compared to controls (Figure S8A). For both treatment conditions, we confirmed a decrease in B cells in the spleen while a reduction in T cells was more prominent for the NIK^{inh} single treatment alone than in combination treatment group (Figures 8C and 8D). $CD4^+$ T cells were depleted completely for the Tfh PD-1^{high} population in the combination treatment group, while a residual subpopulation of PD-$1^{high}CD4^+$ cells was detected in NIK^{inh} only treated mice (Figure 8E). The $CD4^+$ clonality for TCR-β7 detected in the initial tumor was not detected as dominant in the NIK^{inh} + anti-PD-1 treated mice, but TCR-β7 dominance was still present in residual $CD4^+$ cells for the single NIK^{inh} treatment (Figure S8B). Additionally, expression of non-canonical NF-κB pathway components and targets was reduced in residual $CD4^+$-T cells following combined NIK^{inh} and anti-PD-1 treatment, demonstrating the efficacy of NIK^{inh} to inhibit the non-canonical NF-κB pathway *in vivo* (Figure S8C). In the double treated group, anti-PD-1-mediated induction of immune response was confirmed by increased production of

IFNγ, granzyme B and perforin by cytototoxic $CD8^+$ cells, while the NIK^{inh} alone was capable of increasing IFNγ release but not granzyme B and perforin (Figure 8F). Of note, PD-1 was highly expressed on $CD4^+$ but not $CD8^+$ T cells in the primary mPTCL, while CD4 Tfh, CD8 T cells and GC B cells expressed PD-L1 at high levels (Figure S8D), suggesting that anti-PD-1 treatment may not only disrupt T-T cell interactions but also T-B cell interactions, known as drivers of T and B cell proliferation in PTCL. Therefore, we evaluated anti-PD-1 treatment alone. Anti-PD-1 treated plck-GAPDH mPTCL engrafted mice had significantly increased survival compared to control-treated animals, and two mice survived long-term upon continuous treatment (Figure S8E). A strong depletion of $CD4^+$ T cells was detected in the spleen (Figure S8F), while $CD8^+$ cells were unaffected (data not shown), resulting in a reduced $CD4^+/CD8^+$ ratio (Figure S8G). In contrast, anti-PD-1 treatment increased the percentage of B cells in the spleen but decreased the percentage of GC B cells as compared to control treatment (Figure S8H and S8I). As for the combination treatment (NIK^{inh} +anti-PD-1), anti-PD-1 treatment stimulated an immune response as confirmed by increased production of IFNγ, granzyme B and perforin by cytotoxic $CD8^+$ T cells (Figure S8J).

To further emphasize the relevance of NIK inhibition in hAITL, we isolated $CD4^+$ T cells from human AITL tumor samples. As detected in our mAITL tumors, the hAITL $CD4^+$ T cells showed a Tfh phenotype ($PD\text{-}1^{high}$, $ICOS^+$ $CXCR5^+$) and B cells demonstrated a GC B cell ($GL7^+$) phenotype (data not shown). Both cell types showed strong upregulation of NIK (up to 8-fold) in most cases compared to their healthy counterparts (Figures 8G and 8H). We clearly demonstrated that NIK^{inh} treatment *ex vivo* reduced the growth of $CD4^+$ Tfh cells from hAITL biopsies upon TCR stimulation, whereas healthy $CD4^+$ T cells remained unaffected (Figure 8I). The response of each donor sample correlated with the level of NIK expression over healthy $CD4^+$ T cell detected, as the hAITL sample expressing low levels of NIK was not affected by the inhibitor (AITL-1 in Figure 8G and 8I). Moreover, the GC B cells in the hAITL samples showed decreased growth upon NIK^{inh} treatment in agreement with their increased NIK expression (Figures 8H and 8J).

These results support that drugs targeting the non-canonical NF-κB pathway represent a potential treatment option for AITL.

Discussion

By overexpressing GAPDH into the T cell lineage, we established here a preclinical plck-GAPDH mouse model of hAITL, a rare T cell lymphoma. AITL is highly resistant to conventional chemotherapy and prognosis is usually poor with a survival rate of only 30% at 5 years (de Leval et al., 2010; Federico et al., 2013). AITL pathology develops at a later age and is characterized by splenomegaly, hepatomegaly, and enlarged LNs. Moreover, a large number of patients develop a skin rash and ascites in the abdomen (de Leval et al., 2010). All these features were detected in our mPTCL. Clonal Tfh cell tumor infiltration is one of the hallmarks of hAITL, and Tfh are possibly at the origin of this disease (Crotty, 2014; de Leval et al., 2007; Dupuis et al., 2006; Grogg et al., 2006). However, this T cell component represents only a fraction of the tumor mass and is always accompanied by GC B and/or plasma B cells and FDCs (Gaulard and de Leval, 2014; Mourad et al., 2008). Thus, hAITL is a complex malignancy, in which the tumor microenvironment is a key element. Tfh cells associate with B cells in the GC, where they sustain GC B cell survival and T-B cell connection through ligand-receptor interactions (PD-1-PD-L1, ICOS-ICOSL, FAS-FASL). Remarkably, a cytokine-chemokine secretion pattern was revealed in hAITL (Heissmeyer and Vogel, 2013; Stone et al., 2015; Weber et al., 2015a) and confirmed in our mPTCL. Moreover, our mPTCL manifests autoimmunity-like symptoms consistent with hAITL (de Leval et al., 2007). Most strikingly, GAPDH was increased in AITL patient LNs, stressing the equivalence of our model with AITL. How GAPDH is modulated in such a lymphoma still needs to be unraveled. GAPDH overexpression strongly induced the canonical NF-κB pathway in the plck-GAPDH thymocytes. This might lead to aberrant T cell development since NF-κB is implicated in thymocyte development (Gerondakis et al., 2014; Xing et al., 2016). Moreover, constitutive canonical NF-κB activation creates an inflammatory context (Hoesel and Schmid, 2013), which might be prosperous for induction of genetic mutations.

In 50-70% of AITL patients the Ras homolog gene family member A (*RHOA)* bears a G17V mutation (Palomero et al., 2014; Sakata-Yanagimoto et al., 2014). This results in the loss of function of the RHOA GTPase and is often associated with TET2 loss of function mutations in hAITL (Palomero et al., 2014; Yoo et al., 2014). Genetic mouse models have been proposed to mimic hAITL such as the TET2-KD mouse (Muto et al., 2014) and the SJL mouse driving T cell lymphoma due to elevated IL-21 levels (Jain et al., 2015). However, both of the models only recapitulate part of hAITL. Recently, two double *TET2*$^{-/-}$ *RHOA*^{G17V} mouse models were generated recapitulating AITL disease more closely (Cortes et al., 2018; Ng et al., 2018). Strikingly, we revealed also *RHOA* mutations in our murine plck-GAPDH AITL disease model.

The connection between GAPDH overexpression and NF-κB activation was revealed previously by us (Chiche et al., 2015). NF-κB deregulation is found in many hematological malignancies (Imbert and Peyron, 2017) and other cancers (De Donatis et al., 2016; Fradet et al., 2004; Karin et al., 2002; Madonna et al., 2012). Importantly, increased NF-κB activation may induce tumour immune escape and chemotherapy resistance (Burstein and Duckett, 2003; Fujioka et al., 2012). Therefore, NF-κB is currently considered an ideal target for cancer therapy, and various NF-κB inhibitors targeting different pathway components are under development (Shen and Tergaonkar, 2009).

The constitutive canonical NF-κB activation might have contributed to the activation of the non-canonical pathway in pre-malignant and malignant plck-GAPDH T cells. This was previously described in LN formation underlining the interdependency of these two NF-κB pathways (Alcamo et al., 2002; Lo et al., 2006; Shih et al., 2011). Genetically manipulating the NF-κB pathway in mice showed the interdependence of the canonical and non-canonical pathways and the importance of the initial induction of the canonical NF-κB pathway by GAPDH followed by the non-canonical pathway in accelerated Tfh development.

EZH2 is increasingly expressed during the progression of hematopoietic and solid cancers (Bachmann et al., 2006; Chen et al., 2018; Karakashev et al., 2018; Patnaik et al., 2018; Sudo et al., 2005) and overexpression of mutant EZH2 has been recognized in a wide selection of B and T cell lymphoproliferative disorders (Morin et al., 2010; Raaphorst et al., 2000; Sasaki et al., 2011; Sneeringer et al., 2010; Visser et al., 2001). Therefore, considerable effort has been directed toward development of EZH2 inhibitors but current specific EZH2 inhibitors can results in either pro-oncogenic or tumor-suppressive effects (Lund et al., 2014). EZH2 inhibitors are catalytic inhibitors that only act on the enzymatic activity of EZH2. By acting on NIK we can decrease EZH2 at the transcriptional level. Thus, NIK inhibitors would inhibit the catalytic and non-catalytic effect of EZH2. Indeed, EZH2 inhibits IFNγ production at the transcriptional level (Wee et al., 2014), which is essential for the anti-PD-1 response. Moreover, the non-canonical pathway has pro-oncogenic effects by itself and targeting NIK will decrease EZH2 but also the non-canonical NF-κB pathway.

We demonstrated that the non-canonical pathway is highly activated in hAITL equivalent to our mAITL model. Of note, a major component in our murine and human AITL are GC B cells, which also have the non-canonical NF-κB pathway constitutively activated (Gardam et al., 2008; Sun, 2017; Xie et al., 2007). Of importance, NIK is required for maintaining high expression of ICOSL on B cells, important for Tfh generation (Hu et al., 2011). We

confirmed overexpression of NIK in hAITL Tfh cells and GC B cells compared to their healthy counterparts, and the NIK^{inh} strongly increased survival of our mAITL preclinical model. Altogether, this argues strongly for interference of the non-canonical NF-κB pathway as a treatment for AITL-like disease.

PD-1 is a checkpoint receptor that upon engagement by PD-L1 dampens T effector functions and protects cancer cells from immune-mediated attack (Kleffel et al., 2015; Topalian et al., 2012). Thus, antibodies targeting the PD-1-PD-L1 interaction have been developed and are currently used clinically in treating cancer patients (Postow et al., 2015; Topalian et al., 2016; Weber et al., 2015b). Anti-PD-1 treatment led to a decrease in $CD4^+$ T cells in engrafted plck-GAPDH tumors and boosted $CD8^+$ T cell activity. As for melanoma, the Tfh cancer cells might also be directly targeted by anti-PD-1 by a cell-intrinsic mechanism (Kleffel et al., 2015).

Treatment with NIK^{inh} induced IFNγ secretion, which might augment the response to the anti-PD-1 immunotherapy (Fu et al., 2014; Guo et al., 2015). Moreover, IFNγ derived from cytotoxic lymphocytes enhances their motility and cytotoxicity (Bhat et al., 2017). However, combined NIK^{inh} with anti-PD-1 treatment did not further increase survival compared to NIK^{inh} alone. The double treatment did result in $CD4^+$ T cells, which were devoid of PD-1 expression, in contrast to the residual $CD4^+$ T cell upon NIK^{inh} alone, which still expressed PD-1.

Importantly, NIK^{inh} treatment inhibited growth of hAITL $CD4^+$ Tfh and GC B cells *ex vivo*, further emphasizing the role of the non-canonical NF-kB pathway in hAITL and the relevance of NIK inhibition for this disease that is in need of better optimized therapies.

In summary, we have established that the plck-GAPDH mice develop AITL recapitulating the pathology, the transcriptional profile and genetic and immune-phenotypic features of hAITL. This mAITL model will help to unravel the possible origin of the disease and pathways implicated and will permit us to test therapeutic options. Here we provide evidence for the potential utility of immunotherapies and small molecule inhibitors of NIK and combinations thereof for treating AITL.

Acknowledgments

We acknowledge animal and confocal facilities at the C3M (INSERM U1065, Nice, France). This work was supported by the 'Fondation ARC pour la Recherche sur le Cancer' and 'the Agence Nationale de la Recherche' (Labex SIGNALIFE ANR-11-LABX-0028-01), the

Canceropôle PACA, Institut National du Cancer (INCA) and Conseil Régional PACA and the French Ministry of Research. LM was supported by 'la Fondation pour la Recherche Médicale (FRM)' and 'Aides individuelles aux jeunes chercheur ville de Nice'. RM was supported by a PhD fellowship from the French Ministry of Research.
RNA-Seq sequencing experiments were performed at the UCAGenomiX (IPMC), Sophia-Antipolis, Nice, France). Sequencing at UCAGenomiX (IPMC), a partner of the National Infrastructure France Génomique, was supported by Commissariat aux Grands Investissements (ANR-10-INBS-09-03, ANR-10-INBS-09-02) and Canceropôle PACA. We thank the platform of Experimental Histopathology at INSERM/UPS US006 CREFRE, Toulouse Purpan, France. For bioinformatic analysis we thank Nicolas Nottet (C3M, INSERM U1065, Nice, France). For cloning we thank Patrick Munro. hAITL cells were obtained from the INCA labelled Tumorotek of Necker-Enfants Malades Hospital, Paris France.

Author contributions

EV coordinated the project, designed and performed experiments, analyzed and discussed the data, and wrote the manuscript; JER designed experiments and wrote the manuscript; LM., RM, GD designed and performed experiments, analyzed and discussed the data, and wrote the manuscript; MT., CP, LB, AD, FL, JGN, LS, NF, FC, NJC, MJ, VI, EP, CRP, JPB, FM, SM, E Villa performed experiments, analyzed the data, discussed results. VA, PG and F. Lemonnier provided AITL patient cells and discussed the data; PD, AM synthesized anti-NIK inhibitors, discussed results; JFP, LG, RB, JJF, TP provided critical discussions and reading of the manuscript.

Supplemental information

Supplemental information includes 8 figures and 7 tables.

Declaration of interest

NIK inhibitor compounds are under licensing by YUKIN therapeutics. Rachid Benhida and Thierry Passeron are co-founders of YUKIN therapeutics. The remaining authors declare no conflict of interest.

Figure Legends

Figure 1. Overexpression of GAPDH in the T cell lineage does not affect early T cell development.

(A) Schematic presentation of the GAPDH expression construct to generate 3 founder mice (F16, F35, F07). Plck: lymphocyte-specific protein tyrosine kinase promoter; V5: tag for FACS and western blot detection. (B) Western blot using an anti-V5 antibody for GAPDH-V5 detection and anti-GAPDH for detection of endogenous GAPDH and GAPDH-V5 in plck-GAPDH transgenic (Tg 1 and Tg 2) or WT (WT 1 and WT 2) 5-week old mice. (C) Intracellular GAPDH-V5 and GAPDH detection in T cells ($CD3^+$) and in B cells ($CD19^+$) from the spleen analyzed by FACS in 5-week old mice. (D) Ectopic GAPDH-V5 expression levels (mean fluorescence intensity, MFI) detected by FACS using anti-V5 antibody in thymocyte subpopulations: double negative, DN ($CD4^-CD8^-$); double positive, DP ($CD4^+CD8^+$); $CD4^+$ ($CD8^-CD4^+$) and $CD8^+$ ($CD4^-CD8^+$) cells from WT (n=18) and 3 founder plck-GAPDH mice at 5 weeks (F07, n=7; F16, n=15, and F35, n=13, mean ± SD, $p< 0.001$, one way ANOVA for all the groups). (E) Total GAPDH expression levels (MFI) detected by FACS using anti-GAPDH antibody in the DN, DP, $CD4^+$ and $CD8^+$ thymocytes for WT (n=18) and 3 founder plck-GAPDH mice (F07, n=7; F16, n=15, and F35, n=13, mean ± SD, ** $p< 0.0$, one way ANOVA) at 5 weeks of age. (F) Distribution of DN, DP, $CD4^+$ and $CD8^+$ thymocytes analyzed by FACS in WT and plck-GAPDH mice and thymocyte cell numbers are summarized in a histogram (mean ± SD, n=5).

Figure 2. Aged plck-GAPDH mice develop a PTCL-like lymphoma

(A) Frequency of tumor appearance among the different plck-GAPDH founder mice (20/20 for F07; 20/20 for F35; 6/16 for F16; 2/23 for WT). (B) Cumulative incidence of tumor development in plck-GAPDH mice from the founders F07 and F35 according to their age (plck-GAPDH, n=40 and WT, n=30). (C) Frequency of tumor localization in plck-GAPDH mice. Ectopic LN were localized at kidney, thymus, and intestines. (D-F) Weight of spleens

(D), mesenchymal LNs (MES LN) (E) and ectopic LNs (F) of WT mice and plck-GAPDH mice presenting tumors (means ± SD, n=24; *** p<0.001; ** p< 0.01, student t-test).
(G) Representative pictures of spleen, MES LN and liver of WT and plck-GAPDH mice presenting tumors. (H) Hematoxylin and eosin staining patterns and IHC staining for $CD3^+$ T cells and $B220^+$ B cells of WT and plck-GAPDH spleens.
(I-J) Numbers of B ($CD19^+$) and T ($CD3^+$) cells (I) and the ratio of $CD4^+/CD8^+$ T cells (J) in the spleens of WT and plck-GAPDH tumor bearing mice (means ± SD, n=6; *** p<0.001 ; *p<0.05, student t-test). See also Figure S1.

Figure 3. Plck-GAPDH mice developed a T-cell lymphoma with a pronounced Tfh phenotype

(A) Comparison of Tfh cell ($CD4^+CXCR5^+$ PD-1^{high}; $CD4^+CXCR5^+Bcl\text{-}6^+$ and $CD4^+ICOS^+$) infiltration in the spleen of plck-GAPDH and WT mice analyzed by FACS. Representative of n=10. Initial gating on $CD4^+$ cells is performed. (B) Percentages of $CD4^+$ T cells that are PD-1^{high} $CXCR5^+$PD-1^{high} T cells in WT and plck-GAPDH spleens (means ± SD, n=10; ***p<0.001, student t-test). (C) $CD4^+$ T cell staining for CD62L and CD44 in plck-GAPDH tumors and WT spleens by FACS. Representative of n=6. (D) Expression of FAS receptor (CD95) and FAS ligand (CD178) on $CD4^+$ T cells by FACS. Representative of n=6. (E) Intracellular staining of Ki67 in $CD4^+$ splenocytes by FACS. Representative of n=3. (F) Intracellular marking of IFNγ, IL-10 and TNFα in $CD4^+$ splenocytes upon PMA/ionomycin stimulation in WT and plck-GAPDH mice. Representative of n=4. (G) Expression of the different TCR-β chains on WT (WT 1, WT 2) and plck-GAPDH (GAPDH 1, 2, 3) $CD4^+$ T cells analyzed by FACS. (H) Detection of different TCR-γ chains by PCR in $CD4^+$ splenic cells isolated from WT (lane 1 to 3) or plck-GAPDH lymphoma bearing mice (lane 4 to 8).

Figure 4. Germinal center B cells are strongly increased in plck-GAPDH tumors.

(A) GC B cells identified by FACS using staining for FAS (CD95) and GL-7 gated on $CD19^+B220^+$ B cells. Representative of n=10. (B) % of GC B cells on $CD19^+B220^+$ cells in WT and plck-GAPDH spleens and MES LN (mean ± SD; spleen, n=38; LN n=20; ***p<0.001, student t-test) (C) Representative FACS plot showing the expression levels (MFI) of FAS ($CD95^+$) and FAS ligand ($CD178^+$) in WT *vs* plck-GAPDH B cells ($CD19^+B220^+$). Representative of n=5. (D) FACS histogram showing the quantity of

plasmocytes (CD19-B220 low, $CD138^+$) per total nucleated cells in the spleen. (E) Summary of the percentage of plasma B cells from (D) (mean ± SD, n=22; **p<0.01, student t-test).
(F, G) Total splenocytes from tumor bearing plck-GAPDH mice were transferred to NSG mice, which were sacrificed 6-8 weeks post-injection. PD-1^+ $CD4^+$ T cells and GC B cells ($CD95^+$GL-7^+) in donor plck-GAPDH mice and in NSG mice after engraftment were analyzed by FACS (F), and the percentages of $CD4^+$ T cells that were PD-1^+ and B cells that were $CD95^+$GL-7^+ were quantified for 3 independent tumors (G). See also Figure S2.

Figure 5. Plck-GAPDH mPTCL transcriptional profile corresponds to that of AITL patients

(A) mRNA expression (log^2) of Tfh signature genes based on gene expression analysis (GEA) of RNAseq data in total splenocytes of lymphoma developing plck-GAPDH relative to WT splenocytes. (B) GSEA for 18 Tfh related genes indicated in A. For all genes with enrichment score > 0 (black bars in the pink zone) expression is upregulated. KS-test (C) mRNA expression levels by Q-PCR analysis of CXCL13, IL-21, Bcl-6 and BLIMP in $CD4^+$ T splenocytes isolated from plck-GAPDH mPTLC and WT mice. Expression for WT was set to 1 (mean ± SD, n=3; *p<0.05, **p<0.01, student t-test). (D) mRNA expression levels (log^2) of GC/plasma B cell signature genes based on the GEA of RNAseq data in plck-GAPDH relative to WT splenocytes. (E) GSEA for GC/plasma B cell related genes presented in D. For all genes with enrichment score > 0 (black bars in the pink zone) expression is upregulated. KS-test. (F) mRNA expression level (RNAseq data) of GAPDH (log^2) in $CD4^+$ T splenocytes isolated from plck-GAPDH mPTLC as compared to WT splenocytes (Boxplots represent the 25th and 75th percentiles with midlines indicating the median values; Whiskers extend to the maximum/minimum values of the data samples) (**p<0.01, student t-test) and GAPDH intracellular staining in $CD4^+$ mPTCL and healthy splenocytes analyzed by FACS. (G) mRNA expression levels (RNAseq data) of GAPDH in LN from AITL and healthy donors (Boxplots represent the 25th and 75th percentiles with midlines indicating the median values; Whiskers extend to the maximum/minimum values of the data samples; *** p<0.001, student t-test). (H) Metabolic pathway analysis from RNAseq data of the plck-GAPDH lymphoma vs WT splenocytes was performed using the KEGG database. *p < 0.05; ns: non significant, See also figures S3 and S4, tables S1 and S2.

Figure 6. *RHOA* mutations and other mutations identified in plck-GAPDH Tfh mPTCL

(A) Sanger sequencing of isolated mPTCL lymphoma $CD4^+$ cells identified a *RHOA* single

bp mutation (T37M) and INDEL (frameshift insertion) mutation. The T37M mutation was detected in 15 out of 15 different plck-GAPDH mice and the INDEL in 4/15 plck-GAPDH mice.

(B) Active RHOA (Rho-GTP) was compared using a GST-rhotekin RBD pull down assay using lysates of HEK293T transfected with WT and different RHOA inactivating mutants (T37M, T37A, T19N) or a RHOA activating mutant (Q36L)

(C) *RHOA* mutations in patients according to published data for AITL (Vallois et al., 2016), PTCL (Palomero et al., 2014), adult T cell leukemia/lymphoma (ATL; (Nagata et al., 2016)), follicular lymphoma (Zehir et al., 2017), Burkitt lymphoma (Rohde et al., 2014) and Gastric carcinoma (Kakiuchi et al., 2014). Each symbol represents a patient for the indicated mutation and the number of symbols represent the frequency of that mutation found per total number of patients (n) analyzed. See also Figure S5 and Tables S3-S6.

Figure 7. Plck-GAPDH AITL tumors show a strong activation of the non-canonical NF-κB pathway in Tfh cells.

(A) Heatmap for GEA data of canonical (blue) and non-canonical (green) NF-κB pathway and target genes comparing total splenocytes from WT and lymphoma cells from plck-GAPDH mice. (B) GSEA for these NF-κB related genes in A. For all genes with enrichment score > 0 (black bars in the pink zone) expression is upregulated. KS-test. (C, D) mRNA expression levels in $CD4^+$T cells of plck-GAPDH vs WT mice for the canonical pathway genes (NF-κB1 and RelA) and target genes (NF-κBia, E2F1 and GADD45) (C) and noncanonical pathway genes (NF-κB2, RelB) and target genes (EZH2, SP-1, IRF4, ENPP2) (D) (mean ± SD, n=3; *p<0.05, **p<0.01; ***p<0.001; student t-test). (E, F) Heatmaps of transcriptomic data comparing healthy (n=8) and hAITL (n=52) LNs for their NF-κB canonical pathway genes (NF-κB1 and RelA) and target genes (NF-κBia, E2F1 and GADD45) (E) and non-canonical pathway genes (NF-κB2, RelB) and target genes (EZH2, SP-1, IRF4, ENPP2) (F) (Healty n=8; AITL n=60). (G) plck-$I\kappa B^{-/-}$, plck-$p65^{-/-}$ and WT mice were sacrificed at 18 months and splenocytes were analyzed by FACS for Tfh markers (PD-1^+CXCR5^+ gated on $CD4^+$), GC B markers ($CD95^+$, GL-7^+ gated on $CD4^+$), $CD4^+/CD8^+$ ratio (gated on $CD3^+$), and GAPDH expression. (H) mRNA expression levels of Tfh signature genes by Q-PCR in $CD4^+$ T splenocytes isolated from plck-$I\kappa B^{-/-}$ or WT mice. Expression of WT was set to 1 (mean ± SD, n=3; *p<0.05, **p<0.01; student t-test). See also Figure S6.

Figure 8. Combining NIK Inhibition and anti-PD-1 prolongs survival of the AITL mouse model

(A) mRNA expression levels by Q-PCR of NIK in $CD4^+$ T and $CD19^+$ B cells from lymphoma developing plck-GAPDH mice as compared to cells from WT spleens, set to 1 (mean ± SD, n=3; **p<0.01; ***p<0.001, student t-test).

(B) Splenic lymphoma cells from plck-GAPDH mice were injected IV into recipient NSG mice (n= 18), which were treated with vehicle (n=5), a NIK inhibitor (NIK^{inh}; n=6), and NIK^{inh} + anti-PD-1 (n=7). Survival curves for mice are shown. Mice were sacrificed at 90 days post-transplant (** p<0.01, * p<0.05, Mantel-cox test).

(C) Percentage of B cells ($CD19^+$) and T cells ($CD3^+$) in the spleen per total mononuclear cells for the indicated treatment groups at sacrifice (mean ± SD, n=4; *** p<0.001, **p<0.01, * p<0.05, one way ANOVA)

(D-E) Ratio of $CD4^+/CD8^+$ T cells (D) and percentage of PD-1^{high} $CD4^+$ T cells (E) in the spleen for the indicated treatment groups at sacrifice (mean ± SD, n=4; *** p<0.001, **p<0.01, one way ANOVA).

(F) Splenocytes isolated from NIK^{inh}, NIK^{inh} + anti-PD-1 and control treated NSG mice at sacrifice were activated for 5 hr with PMA/ionomycin, then surface-stained for CD8 followed by intracellular staining for IFNγ, perforin and granzyme B (mean ± SD, n=3; *p<0.05, **p<0.01, ***p<0.001, one way ANOVA).

(G, H) Fold change mRNA expression levels by q-PCR analysis of NIK in human $CD4^+$ T cells (G) and GC B cells (H) isolated from LN biopsies from 5 different AITL patients and in healthy human counterparts, for which expression level was set to 1 (mean ± SD, analysis was performed in triplicate for each AITL sample).

(I, J) Effect of NIK^{inh} (10 μM, 48 hr) on the cell number of $CD4^+$ T cells (I) and GC B cells (J) of LN biopsies from 5 different AITL patients upon TCR-stimulation compared to TCR-stimulated healthy $CD4^+$ human T cells and healthy B cells. Cell numbers are normalized to the corresponding DMSO-treated control cells. See also Figure S7 and S8.

STAR*METHODS

KEY RESOURCES TABLE

REAGENT or RESOURCE	SOURCE	IDENTIFIER ; RRID
Antibodies		

CD3 APCcy7 (145-2C11)	Miltenyi	Cat#130-102-306 ; AB_2660402
CD19 PE (1D3)	BD Pharmingen	Cat# 553786 ; AB_395050
Anti-V5 APC	Abcam	Cat# Ab72560 ; AB_1271439
CD4 FITC (RM4-4)	Miltenyi	Cat# 130-102-541 ; AB_2659902
CD8 PEcy7 (REA601)	Miltenyi	Cat# 130-119-123; AB_2733250
CD44 PE (IM7)	BD Pharmingen	Cat# 553134 ; AB_394649
CD25 APC (PC61.5)	eBioscience	Cat# 47-0251 ; AB_1272215
B220 FITC (REA755)	Miltenyi	Cat# 130-110-845 ; AB_2658273
PD-1 PE (CD279; REA802)	Miltenyi	Cat# 130-111-800 ; AB_2656934
CXCR5 APC (REA215)	Miltenyi	Cat# 130-103-113; AB_2655792
CD62 L APCcy7 (MEL-14)	BD Pharmingen	Cat# 560514 ; AB_10611861
Ki67 PE (REA183)	Miltenyi	Cat# 130-100-289 ; AB_2652551
CD95 VB (Jo2)	BD Pharmingen	Cat# 562633 ; AB_2737690
CD178 PE (MFL3)	Miltenyi	Cat# 130-102-590 ; AB_2655652
INF G APC (XMG1.2)	BD Pharmingen	Cat# 554413 ; AB_398551
IL10 PE (JES5-16E3)	eBiosciences	Cat# 12-7101-81 ; AB_466175
Perforin PE (eBioOMAK-D)	eBiosciences	Cat# 12-9392-82 ; AB_466243
IL-4 APC (11B11 Ruo)	BD Pharmingen	Cat# 554436 ; AB_398556
IL-17 PE (TC11-18H10)	BD Pharmingen	Cat# 559502 ; AB_397256
Granzyme B PEcy7 (NGZB)	eBiosciences	Cat# 25-8898-82 ; AB_10853339
TNFα FITC (MP6-XT22)	BD Pharmingen	Cat# 557719 ; AB_396828
F4/80 VB (BM8)	eBiosciences	Cat# 48-4801-82 ; AB_1548747
CD11c PE (HL3)	BD Pharmingen	Cat# 560521 ; AB_1727423
GL-7 APC (GL7)	BD Pharmingen	Cat# 561529 ; AB_10716056
CD138 APC (REA104)	Miltenyi	Cat# 130-102-528 ; AB_2655022
PD-L1 PEcy7 (MIH5)	eBioscience	Cat# 25-5982-80 ; AB_2573508
ICOS-VB (CD278; REA192))	Miltenyi	Cat# 130-100-639 ; AB_2656917
ICOSL APC (CD275; HK5.3)	Miltenyi	Cat# 130-102-944 ; AB_2656899
CD19 FITC (6D5)	Miltenyi	Cat# 130-102-494 ; AB_2661108
Ter119 FITC (TER-119)	Miltenyi,	Cat# 130-102-257 ; AB_2660080
NK1.1 FITC (PK 136)	BD Pharmingen	Cat# 553164 ; AB_394676
CD49b FITC (DX5)	BD Pharmingen	Cat# 553857 ; AB_395093
Ly6C FITC (RB6-8C5)	BD Pharmingen	Cat# 553127 ; AB_394643
CD11c FITC (HL3)	BD Pharmingen	Cat# 553801 ; AB_395060
CD4 FITC (clone MT466)	Miltenyi	Cat#130-113-815 ; AB_2726332
CD19 FITC (clone LT19)	Miltenyi	Cat#130-113-165 ; AB_2725993
CD122 FITC (5H4)	BD Pharmingen	Cat# 554452 ; AB_395401
Anti- Lck pY505 APC	Miltenyi	Cat# 130-110-285 ; AB_2652607
Anti-ZAP70 (PY319)/Syk (PY352)	BD Biosciences	Cat# 557817 ; AB_396884
Anti-Erk1/2; Thr202/Tyr204	Cell signaling	Cat# 4370 ; AB_2315112
CD69 APC-efluor 780	eBioscience	Cat# 47-0691-82 ; AB_2573966
CD25-FITC	Miltenyi	Cat# 130-104-275 ; AB_2660257
Rabbit anti-murine IFNγ	Peprotech	Cat# 500-P119 ; AB_147751
Rabbit anti-murine IL-4	Peprotech	Cat# 500-P54 ; AB_147969
Mouse anti-TGFBeta (1,2,3) 51D11)	R&D Systems	Cat# MAB1835 ; AB_357931
Mouse Vβ TCR screening panel (FITC)	BD Biosciences	Cat# 557004 ; AB_647180

Rabbit mAb Hsp90 (C45G5)	Cell signaling	Cat# 4877S ; AB_2233307
Rabbit mAb p NF-kappa B2 p100 (S866)	Cell signaling	Cat# 4810S ; AB_659925
Rabbit mAb p-IKKalpha (S176)/IKKbeta (S177)	Cell Signaling	Cat# 2078S ; AB_2079379
Rabbit mAb anti-GAPDH	Abcam	Cat# ab9485 ; AB_307275
Mouse mAb NF-κB1	Santa Cruz	Cat# sc-166588X ; AB_2236119
Rabbit mAb PD-1 (PMP1-14)	BioXcell	Cat# BE-0146 ; AB_10949053
Mouse mAb V5tag	Invitrogen	Cat# R96025 ; AB_159313
Rabbit Polyclonal anti-GAPDH	Abcam	Cat# Ab9485 ; AB_307275
Anti CD3 (2GV6) Rabbit monoclonal primary antibody	Roche	Cat# 7904341 ; AB_2335978
Rat Anti-mouse CD45R monoclonal antibody (RA3-6B2)	BioRad	Cat# MCA1258GT ; AB_1102070
Ki67 Monoclonal Antibody (SP6)	Thermofisher Scientific	Cat# MA5-14520 ; AB_10979488
Mouse Monoclonal Anti-Bcl-6	Santa Cruz	Cat# sc-7388 ; AB_2063455
Rabbit Polyclonal Anti CD35	Biorbyt	Cat# orb13316 ; AB_10767957
Anti-CD31 (PECAM)	BD biosciences	Cat# 553373 ; AB_394819
Anti-NF-κB2	Santa Cruz	Cat# sc-7386x ; AB_2267131
Rabbit polyclonal anti-p65	Santa Cruz	Cat# sc-8008x ; AB_628017
Anti- RelB	Santa Cruz	Cat# sc-166416x ; AB_2179178
Rabbit mAb anti-pNF-kappaB p65 (S536)	Santa Cruz	Cat# sc-372 ; AB_632037
Rabbit polyclonal anti NF-kappaB p52	Santa Cruz	Cat# sc-298 ; AB_2151277
Rabbit polyclonal anti-TRAF2	Santa Cruz	Cat# sc-7187 ; AB_793340
Anti-human NF-κB2 p100/p52	Cell Signaling	Cat# 4882 ; AB_10695537
Anti-human EZH2 (D2C9) XP	Cell Signaling	Cat# 5246 ; AB_10694683
Anti-human RelB (C1E4)	Cell Signaling	Cat# 4922 ; AB_2179173
Anti-human NIK	Cell Signaling	Cat# 4994 ; AB_2297422
Mouse mAb anti-rabbit IgG Conformational specific coupled to HRP	Cell signaling	Cat# 5127; AB_10892860
Hamster anti-mouse CD3e (NA/LE)	BD Pharmingen	Cat# 553057 ; AB_394590
Hamster anti-mouse CD28 (NA/LE)	BD Pharmingen	Cat# 553294 ; AB_394763
Biological Samples		
AITL patient biopsies	This manuscript Tumorotek Necker – Enfants Malades Hospital (Paris, France)	N/A
Patient Melanocytes	This manuscript	N/A
Chemicals, Peptides, and Recombinant Proteins		
NIK-inh	PCT/EP2017/067306	This manuscript
RPMI medium 1640	Life Technologies	Cat# 61870044
Fetal Bovine Serum	Life Technologies	Cat# 10270-106
Glucose	Sigma	Cat# G6152
L-glutamine	ThermoFischer	Cat# 25030081
Sodium pyruvate	ThermoFischer	Cat# 11360088
Cell Tack	Fisher Scientific	10317081
PMA (phorbol 12-myristate-13-acetate)	Sigma	Cat# P8139

Ionomycin	Sigma	Cat# I0634
Golgi-Plug protein Transport inhibitor	BD Biosciences	Cat# 555029
Oligomycin	Sigma	Cat# O4876
Koningic acid	Clinisciences	Cat# AG-CN2-0118
B-Nicotinamide adenine dinucleotide hydrate (NAD)	Sigma	Cat# N1636
Sodium arsenate	Sigma	Cat# A6756
D-glyceraldehyde-3-phosphate	Sigma	Cat# G5376
Sodium pyrophosphate tetrabasic decahydrate $Na_4P_2O_7$	Sigma	Cat# S9515
CFSE	BD Biosciences	Cat# 565082
2-desoxyglucose	Toronto Research Chemicals	Cat# D239000
Carbonyl cyanide 4-(trifluoromethoxy)phenylhydrazone FCCP	Santa Cruz	Cat# sc-203578
Rotenone	Sigma	Cat# R8875
Antimycin A	Sigma	Cat# A8674
2-NBDG	Fischer Scientific	Cat# N13195
Recombinant Human IL2	Preprotech	Cat# 200-02
Recombinant Mouse IL6	Peprotech	Cat# 216-16
Recombinant Mouse IL21	Peprotech	Cat# 210-21
Critical Commercial Assays		
G-Sepharose 4B conjugate beads	Life technologies	Cat# 101242
Cytofix/Cytoperm kit	BD Biosciences	Cat# 554714
Flexi Tube Gene Solution siRNA-NF-kB2	Qiagen	Cat# GS4791
Flexi Tube Gene Solution siRNA-NIK	Qiagen	Cat# GS9020
Negative control siRNA	Qiagen	Cat#SI03650325
ECL Detection kit	GE Healthcare	Cat# RNP2106
ADP-Glo™ kinase assay	Promega	Cat# V6930
Anti-FITC microbeads kit	Miltenyi	Cat# 130-048-701
RNeasy mini kit	Qiagen	Cat# 74104
Omniscript RT kit	Qiagen	Cat# 205113
Nucleospin Tissue Kit	Macherey Nagel	Cat# 740901
Power Sybr™ Green PCR Master Mix	Thermofisher Scientific	Cat# 4368577
Taqman Fast Universal PCR Master Mix	Fisher Scientific	Cat# 4366072
ELISA Mouse mAb Isotyping Kit	Thermofisher Scientific	Cat# 37503
PE Mouse Anti-Ki67 set	BD Pharmingen	Cat# 556027
Proteome Profiler Mouse Cytokine Array Kit, Panel A	R&D systems	Cat# ARY006
Milliplex MaP Kit 96-well plate assay	Millipore Corporation-Merck	Cat# MCYTOMAG-70K
Streptavidine Magnetic beads	Roche	Cat# 11 641 778 001
Pan T cell isolation kit	Miltenyi	Cat #130-096-535
T cell Transact beads, human	Miltenyi	Cat# 130-111-160
Deposited Data		
RNAseq- sequencing data	This manuscript	GSE121748 ; yjmnaqagjnwxrcn
Whole exome sequencing data	This manuscript	GSE121748 ; yjmnaqagjnwxrcn ; PRJEB11861

Experimental Models: Cell Lines		
A375	ATTC	Cat# CRL-1619
C12.06	This manuscript	N/A
A549	ATTC	Cat# CCL-185
Karpas 422	ECACC	06101702
U-2932	DSMZ	ACC 633
SU-DHL-6	DSMZ	ACC 572
Experimental Models: Organisms/Strains		
Mouse: plck-GAPDH+/- (C57BL/6)	This manuscript	N/A
Mouse: C57BL/6	ENVIGO France	N/A
Mouse: plck-Cre (C57BL/6)	Jackson labs	003802
Mouse: IκB$^{flox/flox}$(C57BL/6)	Rupec et al., 2005	N/A
Mouse: plck IκB-/-(C57BL/6)	This manuscript	N/A
Mouse: p65$^{flox/flox}$	Algul et al., 2007	N/A
Mouse: plck p65-/-	This manuscript	N/A
Mouse: NOD.Cg-Prkdcscid Il2rgtm1Wjl/SzJ	Jackson labs	005557
Oligonucleotides		
Primers (See Table S7)	This manuscript	N/A
HIF Taqman gene expression assay	Thermofisher Scientific	Mm00468878_m1
LDH Taqman gene expression assay	Thermofisher Scientific	Mm00495282_g1
Recombinant DNA		
Plck-hGH-GAPDH-V5	This manuscript	N/A
Software and Algorithms		
Flowjo 10.2	Flowjo	https://www.flowjo.com/solutions/flowjo
Macsquantify Version 2.11	Miltenyi	N/A
Multigauge software	Fuji Film	N/A
xPONENT sofware	Luminex Corporation	https://www.luminexcorp.com/xponent/
Prism 7	Graphpad	https://www.graphpad.com/scientificsoftware/prism/
Pannoramic Viewer	3DHistec	https://www.3dhistech.com/pannoramic_viewer
KEGG data base	N/A	https://www.ncbi.nlm.nih.gov/pubmed/10592173.
C5 data base	N/A	http://www.geneontology.org/page/go-citation-policy
Other		
Sanger sequencing	Biofidal, France	www.biofidal.com
Whole exome sequencing	Novogene, China	HTTP://EN.NOVOGENE.COM

Lead contact and materials availability

Further information and requests for resources and reagents should be directed to and will be fulfilled by the lead contact, Els Verhoeyen (els.verhoeyen@unice.fr)
The mouse lines generated in this study are available upon request.
There are restrictions to the availability of the NIK inhibitor compounds due to licensing by YUKIN therapeutics.

Experimental model and subject details

Mice

Mice were bred and maintained under pathogen-free conditions at the local animal facility (C3M, INSERM U1065, Nice, France). All experimental procedures were carried out in compliance with protocols approved by the local ethical and experimentation committee (SBEA, Nice, France, autorisation N° A06088014 and B0608820). At sacrifice, single cell suspensions were prepared from all the hematopoietic organs (spleen, LNs, liver, blood and bone marrow) for further isolation and analysis.

Generation of plck-GAPDH transgenic mice.

The cDNA of human GAPDH fused to the V5 tag in the plasmid pcDNA3 was amplified by PCR and inserted in a plasmid under the control of the promoter of the kinase LCK (plck-hGH (Chaffin et al., 1990)) upon BamHI digestion. The plck-GAPDH-V5 cassette was linearized from this plasmid and microinjected into the pronuclei of oocytes from C57BL/6J mice that were subsequently implanted into gestating females (Service d'experimentation animale et de Transgénèse (SEAT), CNRS, Villejuif, France).
Three transgenic founders (F35, F16, F07) were selected and were bred by serially backcrossing with C57BL/6JOlaHsd mice for at least 12 generations before phenotypic analysis of the mice. C57BL/6J mice for breeding were obtained from ENVIGO (Cannat, France).
Genotyping of the plck-GAPDH mice was performed on genomic DNA isolated from a tail biopsy using the following couples of primers: S1 = 5' GAGGGAACCCAGTCAGGAGC 3'

and 5' TTGATTTTGGAGGGATCTCG 3' and S2 = 5' GTCAGTGGTGGACCTGACCT 3' and 5' GCGCTTACCTGTAGCCATTGC 3'. These primers were used with standard IL-2 primers as controls.

Generation of plck-p65$^{-/-}$ and plck-IκB$^{-/-}$ mice

Plck-p65$^{-/-}$ mice were generated by crossing plck-Cre transgenic mice (Jackson Institute (n°cat #003802) with p65$^{flox/flox}$ mice provided by R. Schmidt (Algul et al., 2007) in our animal facility. Genotyping was performed using following primers: p65loxRV: 5'GAGCGCATGCCTAGCACCAG 3' and p65loxFW: 5'GTGCACTGCATGCGTGCAG 3'; LckCreRV: 5' GCGGTCTGGCAGTAAAAACTATC 3' and LckCreFW: 5'GTGAAACA GCATTGCTGTCACTT '

Plck-IκB$^{-/-}$ mice were generated by crossing plck-Cre transgenic mice with IκB $^{flox/flox}$ mice provided by R. Rupec (Rupec et al., 2005). Genotyping was performed using following primers:

IκB-lox2-FW: GTG GAG TCA GAT GTA GCA CG; IκB-Lox-2-RV: AGA AAG GGA TAA GCC ATG GAG.

Tumor transplantation into NOD/SCIDγc-/- (NSG) mice

NOD/SCIDγc-/- mice (NSG) were obtained from the Jackson Laboratory (#005557) and housed in our local animal facility (C3M, Nice, France).

Single cell suspensions from spleen or LNs of old (> 18 months) plck-GAPDH mice with splenomegaly were injected intravenously (i.v.) into 6-8 week old NSG mice (1-2x10^7 splenocytes per mouse). Recipient mice were sacrificed for evaluation when the mice became weak and/or splenomegaly could be detected (30 to 60 days after injection). The different hematopoietic organs (liver, spleen, blood and bone marrow) were isolated and single cell suspensions were prepared for FACS analysis (see below).

Anti-PD-1 treatment

Two different plck-GAPDH tumors expressing high levels of PD-1 on the CD4$^+$ T cells were injected into 10 NSG mice and the mice were treated with anti-PD-1 antibody (clone PMP1-14, BioXcell (#BE-046); 125 μg in PBS/mouse) or an isotope control antibody daily for the first 2 days post-tumor injection, then every other day.

Treatment with NIK inhibitor

Splenic lymphoma cells from plck-GAPDH mice were injected intravenously into recipient NSG mice (n=18). Six lymphoma engrafted mice were treated with a chemical NIK inhibitor (Figure S14A) at 250 µg in 100 µl NaCl 0.9% /mouse; patent PCT/EP2017/067306), 5 with vehicle (100 µl NaCl 0.9% /mouse) and 7 with NIK^{inh} + anti-PD-1 (clone PMP1-14, BioXcell (#BE-046); 125 µg in PBS/mouse) on day 1 and 2 after tumor cell injection and then every other day.

Recipient mice were sacrificed at endpoint (> 10% weight loss or palpable splenomegaly). Single cell suspensions were prepared from the spleen, BM and liver for immunophenotypic FACS analysis.

Koningic acid treatment in vivo

$2x10^7$ splenic lymphoma cells from plck-GAPDH mice were injected intravenously into recipient NSG mice (n=10). After 3 mice were treated daily by intraperitoneal injection with koningic acid (Clinisciences, #AG-CN2-0118) (1mg/kg) or with vehicle. Recipient mice were sacrificed at endpoints (when reaching >10% weight loss or palpable splenomegaly). Cell suspensions were prepared from the spleen and used for FACS immuno-phenotyping.

Cells

Melanoma cell lines were purchased from the American Tissue Culture Collection (ATCC, Molsheim, France); DLBCL cell lines U-2932 and SU-DHL-6 were obtained from DSMZ, (Germany) while the Karpas 422 were obtained from ECACC (England) and cultured as described with the suggested optimal medium. Human primary melanoma cells were extracted from biopsy specimens of metastatic melanoma obtained from the Department of Dermatology and the Biobank of the University Hospital of Nice, France. All the protocols regarding patients' specimen were reviewed and approved by local ethical committee from University Hospital of Nice; all patients provided informed written consent. Biopsy was dissected and digested for 1–2 hr with collagenase A (0.33 U/ml), dispase (0.85 U/ml) and Dnase I (144 U/ml) with rapid shaking at 37°C. Large debris were removed by filtration through a 70-μm cell strainer. Viable cells were obtained by Ficoll gradient centrifugation. All melanoma cells were cultured in RPMI medium or DMEM (Gibco Life Science, Life Technologies, Grand Island, NY), supplemented with 7% FBS and penicillin-streptomycin 50

μM (Gibco) at 37°C in 5% CO_2. Cells extracted from patients were used for a maximum of 10 passages.

Adult healthy blood samples were collected in sterile tubes containing the anti-coagulant, citrate-dextrose (ACD, Sigma, France). Samples of AITL patients were retrospectively obtained from the onco-hematology laboratory of the 'Necker-Enfants Malades' hospital in Paris (France). The cells were suspended after mechanical dissection of the lymph node biopsy and frozen in DMSO. All human blood and tissues were obtained after informed consent and approval was obtained by the ethical commitees of the hospitals according to the Helsinki declaration. Human T cells were isolated from peripheral adult blood isolated by negative selection using a Pan T cell enrichment Kit (Miltenyi, #130-096-535) according to manufacturer's instructions. TCR-stimulation was performed using anti-CD3+anti-CD28 coated Transact beads (Miltenyi, # 130-111-160) according to manufacturer's instructions and supplemented with hIL-2 (10 ng/ml).

METHOD DETAILS

Western blot analysis

Thymocytes of 5-week old mice or $CD4^+$ splenic T cells were isolated from WT or plckGAPDH mice and lysed using Laemmli buffer for western blot analysis. Proteins were immunoblotted with the indicated antibodies. Immunoblots were visualized (FUJIFILM LAS4000) using ECL Western blotting Detection Reagents (GE Healthcare, #RNP2106) and quantification was performed using ImageJ Software. Mouse anti-V5 was purchased from Invitrogen (#R960-25), rabbit anti-GAPDH from Abcam (# ab9485) and rabit anti-Hsp90 (C45G5; #4875), and pospho-NF-kappaB2 p100 (S866/870; #4810T) from Cell signaling (Leiden, The Netherlands).

Antibodies against murin NF-κB1 (#sc-166588X), NF-κB2 (#sc-7386x), p65 (#sc-8008x) and RelB (#sc-166416x), pospho-p65 (S536; # sc372) were purchased from Santa Cruz (Heidelberg, Germany). Antibodies against human EZH2 (#5246), NF-κB2 (#4882), RelB (#4922) and NIK (#4994) were purchased from Cell Signaling (Leiden, The Netherlands).

Immunoprecipitation

Thymocytes of 5-week old mice were lysed and incubated with G-Sepharose 4B conjugate beads (Life technologies, #101242), pre-absorbed with either 4 μg rabbit anti-TRAF2 from

Santa Cruz (#sc-7187) or 2 µg mouse monoclonal anti-V5 purchased from Invitrogen/ Thermofisher Scientific (#R960-25). Immuno-precipitated proteins were immunoblotted and revealed with mouse anti-rabbit IgG Conformational specific mAb coupled to HRP from Cell Signaling (#5127S).

Flow cytometry and antibodies

Antibodies used for detailed phenotyping or intracellular staining by flow cytometry of T, B and myeloid cells are listed in principle table of the STAR METHODS.

For intracellular staining of Granzyme B, Perforin, IFNγ, TNFα, IL-10, IL-4 and IL-17 splenocytes were stimulated for 5 hours in PMA (phorbol 12-myristate-13-acetate; Sigma, # P8139)/ionomycin (Sigma, # I0634) in the presence of Golgi-stop (BD Biosciences, #555029) and upon surface staining (anti-CD4 or anti-CD8) cells were fixed and permeabilized using the Cytofix/Cytoperm kit and protocol (BD Biosciences; #554714). Intracellular staining for V5tag and GAPDH was performed using the same Cytofix/Cytoperm kit.

All stainings were detected using a MACSQuant flow cytometer (Miltenyi Biotec, Paris, France). Analysis of the FACS data was performed using MACSquantify Version 2.11 (Miltenyi) and FlowJo Software.

Isolation of primary mouse T cells

$CD4^+$ T cells from the spleen of WT or plck GAPDH mice were isolated by negative selection using FITC coupled antibodies: anti-CD19 (Miltenyi, #130-102-494) anti-B220 (Miltenyi, #130-110-845), anti-CD8b (Miltenyi, #130-111-710), anti-Ter119 (Miltenyi, #130-102-257), anti-NK1.1 (BD Pharmingen, #553164), anti-CD49b (BD Pharmingen, #553857), anti-Ly 6C (BD Pharmingen, #553127), anti-CD122 (BD Pharmingen,# 554452) and anti-CD11c (BD Pharmingen, #553801), followed by anti-FITC microbead (Miltenyi, #130-048-701) incubation according to manufacturer's instructions.

Detection of TCR-signaling

$CD4^+$ T cells were activated on NA/LA hamster anti-mouse CD3e (BD Pharmingen, # 553294) coated plates (3 µg) in the presence of NA/LE Hamster anti-mouse CD28 (3 µg/ml; BD Pharmingen, #553294) for 30 min, 6 hr and 24 hr followed by intracellular staining with

anti-Lck pY505 APC from Miltenyi (#130-110-285), alexa fluor 647 mouse anti-ZAP70 (PY319)/Syk (PY352) from BD Biosciences (#557817) or anti-phospho-p44/42 MAPK (Erk1/2; Thr202/Tyr204) from Cell signaling technology (#4370) and analysis by flow cytometry. Intracellular staining was performed by fixation and permeabilization according to manufacturer's instructions.

Activation markers were detected on the $CD4^+$ T cells at 6h and 24h of TCR-stimulation by flow cytometry using surface staining with anti-mCD69APC-efluor 780 purchased from eBioscience (# 47-0691-82) and anti-mCD25-FITC purchase from Miltenyi (#130-104-275). Analysis of the FACS data was performed using Macsquantify Version 2.11 (Miltenyi) and Flojo Software.

Immunohistochemistry analysis and antibodies

Hematopoietic tissues were fixed in formaldehyde overnight and subsequently transferred into 70% ethanol and embedded in paraffin. Hematoxylin and eosin staining were performed on the paraffin embedded tissue sections to color the follicular center. Immuno-staining was performed using anti-mouse antibodies against CD3e (#05493315001, SP7) from Roche, B220 (CD45R) from BioRad (# MCA1258GT), Ki67 (SP6, # MA5-14520) from Thermofisher Scientific, Bcl-6 (Santa Cruz Biotechnology, # sc-7388), CD31 (PECAM-1; 553373; BD Biosciences) and anti-CD35 (Cliniciences, #13316). Adapted secondary antibodies were used for revelation.

Detection of T cell clonality

TCR-β clonality of T cells was determined by surface staining for TCR-β of the $CD4^+$ T cells in the tumors with antibodies directed against the different β-chains (Mouse Vβ TCR screening panel (FITC): mAb against β2, β3, β4, β5.1, β6, β7, β8.1, β8.3, β9, β10, β11, β12, β13, β14, β17; BD Biosciences; #557004).

TCR-γ clonality was detected using specific primers for Vγ1: 3'-CCGGCAAAAAGCAAAAAAGT-5', for Vγ4: 3'- TGTCCTTGCAACCCCTACCCA-5', for Vγ7: 3'- GTGATACTCACAGAACAGGC-5' combined with reverse primer for Cγ 3'-CTTATGGAGATTTGTTTCAGC -5'

Cytokine-chemokine array

Mesenchymal lymph nodes from lymphoma developing plck-GAPDH mice and WT mice used as a control were stimulated for 4 hr with PMA and ionomycin in RPMI/10% FCS at a density of $5x10^6$ cells/ml. Then the supernatant was tested for secreted cytokine and chemokine expression levels using the Proteome Profiler Mouse Cytokine Array Kit, Panel A (ARY006, R&D systems) according to manufacturer's instructions. Quantification was performed using Multigauge (Fuji Film, Tokyo, Japan).

Quantification of Cytokines in mouse serum

Mouse IL-10, IFNγ, IL-1α, IL-1β, IL-6 and TNFα were determined by using the Milliplex MaP Kit 96-well plate assay (MCYTOMAG-70K) according to manufacturer's instructions (EMD Millipore Corporation-Merck, Darmstad, Germany). Detection was performed on the Luminex analyzer MAGPIX® using the acquisition software xPONENT® (Luminex Corporation

Transcriptomic analysis

RNA seq data for plck-GAPDH versus WT mouse splencytes

Total RNA was extracted from splenocytes of tumor developing plck-GAPDH mice and WT mice using the RNA extraction kit (Qiagen, Valencia, CA, USA) according to manufacturer's instructions. Libraries were generated from 500ng of total RNAs using Truseq Stranded Total TNA kit (Illumina). Libraries were then quantified with Qubit dsDNA BR Assay kit (Invitrogen) and pooled. 4nM of this pool were loaded on a high output flow cell and sequenced on a NextSeq500 platform (Illumina) using 2x75bp paired-end chemistry.

RNAseq data were quantified using RSEM sofware 1.2.25 (Li and Dewey, 2011) with bowtie2-2.2.6 and m38 as reference genome.

The gene sets were chosen on the basis of known expression patterns in human and mice Tfh and both GC and post-GC B cell subsets.

AITL patient data

Public raw data AITL transcriptomes using Affymetrix HGU133 Plus 2.0 microarrays were downloaded from GEO dataset (GSE58445 (Iqbal et al., 2014), GSE3526(Roth et al., 2006): GSE7307; https://www.ncbi.nlm.nih.gov/gds) and ArrayExpress (E-TABM-783 (de Leval et al., 2007); https://www.ebi.ac.uk/arrayexpress/), normalized together (RMA) and

collapsed to HUGO gene symbols using chipset definition files.
Expression data were normalized with z-score methods when specified and illustrated with heatmaps using R software (3.3.2). Statistical differences were verified using an unpaired two-tailed Wilcoxon signed rank test versus the specified controls.

Metabolic pathway analysis was performed using the data base KEGG: https:// www.ncbi.nlm.nih.gov/pubmed/10592173. For other signaling/functional pathway analysis we used the data base C5: http://www.geneontology.org/page/go-citation-policy

PCR Amplification and Sanger Sequencing

Mutations in the *RHOA, TET2, IDH2 and DNMT3A* allele were detected in plck-GAPDH tumor cells by PCR amplification using the KAPA HiFi HotStart ReadyMix PCR Kit (Kapa Biosystems, KK2601) and the following primers: RHOA-Fw: CTGCCATCAGGAAGAA ACTGGTG and RHOA-Rv: CTGCTTCCCATCCACCTCGATATC; TET2-Fw: TGGTGGTCACCCTCAATA and TET2-Rv: GAAGACTTTCCCTTCTCAGTC; IDH2-Fw: GTTCAAGCTGAAGAAAATGTGG and IDH2-Rv: CTGGTCGCCATGGGCGTGCC; DNMT3A-Fw: GGGTGTTTGGCTTCCCCGTCC; DNMT3A-Rv: CAGTCACAGCAAG AAACAAAAACC.
The PCR fragments were then sequenced by Sanger sequencing performed at Biofidal (Vaulx en Velin, France; www.biofidal.com).

Determination of GTP levels loaded on RHOA

HEK293T cells were transfected using lipofectamine 2000 (Thermofisher) for 24h with pKH3-HA-RhoA, pKH3 HA-RhoAT37M, pKH3 HA-RhoAT19T or pKH3-HA-RhoAQ63L plasmids. Cells were lysed and levels of active Rho (RhoGTP) in each sample were measured using a GST-rhotekin RBD pull down assay as described previously (Ren and Schwartz, 2000).

***In vitro* Tfh differentiation**

To induce Tfh differentiation in vitro, naive $CD4^+$ T cells were co-cultured with irradiated T cell–depleted splenocytes as co-stimulator cells (irradiated antigen presenting cells) on anti-CD3 coated plates using RPMI media supplemented with 25 ng mL^{-1} IL-6 (#216-16,

Peprotech), 50 ng mL^{-1} IL-21 (#210-21, Peprotech), 4 ng mL^{-1} anti-IFNγ (#500-P119, Peprotech), 4 mg mL^{-1} anti-IL-4 (#500-P54, Peprotech) and 20 mg mL^{-1} anti-TGFB (#1D11, R&D Systems). At several time-points the Tfh differentiation was evaluated by staining with anti-ICOS, anti-PD-1 and anti-CXCR5 antibodies and detection by flow cytometry and also by Q-PCR for Tfh marker (CD21, Bcl-6 and CXCL-13; see star method principle table).

Germinal center induction *in vivo*

To generate germinal center responses and T cell activation, WT mice were immunized with $1x10^9$ sheep red blood cells (SRBC; ORGENTEC, #VSE-410) delivered by intraperitoneal injection every 2 weeks for 4 months.

Reverse transcriptase Quantitative- PCR (RT-qPCR) analysis

$CD4^+$ T cells were isolated from the spleen of tumor bearing plck-GAPDH or WT C57/BL6 mice by incubation of total splenocytes an anti-mouse CD4-FITC antibody (Miltenyi, # 130-102-541) following by an incubation with anti-FITC microbeads (Miltenyi, #130-048-701) according to manufacturer's instructions. $CD19^+$ B cells were isolated using an anti-mouse CD19-FITC (Miltenyi, 130-102-494) antibody and then following the same procedure as for $CD4^+$ cells. Sorting was performed on an autoMACS cell sorter (Miltenyi).

Total RNA was extracted from cells using the RNA extraction kit (Qiagen, #74104, Valencia, CA, USA) according to manufacturer's instructions. Reverse transcription was performed using the Omniscript RT kit (Qiagen, #205113). After reverse transcription-PCR, the relative mRNA expression level of GAPDH, CXCL13, IL-21, BLIMP, Bcl-6, RelA, cRel, GADD45B, E2F1, NF-κBia, HIF-1α, LDHα, NF-κB2, RelB, EZH2, SP1, IRF4, ENPP2, NOD2, 18S (mouse) were obtained by real-time quantification PCR, using SYBR™ Green PCR Mix (Thermofisher Scientific, France) and the corresponding primers sets (see principle table Star methods) on the 7500 Fast and the Step One real-time PCR systems (Applied Biosystems) according to the manufacturer's instructions. All samples were normalized to 18S. The relative mRNA expression level of HIF-1α, and LDHα were obtained by real-time quantification PCR, using the TaqMan PCR Master Mix (Eurogentec, Seraing, Belgium) and TaqMan assay primer set (Thermofisher; HIF-1α,: Mm00468878_m1; LDHα: Mm00495282_g1) on the 7500 Fast and the Step One (Applied Biosystems) according to the manufacturer's instructions. All analyses were performed in triplicate and melting curve analysis was performed for SYBR GREEN to control product quality and specificity.

Genomic DNA isolation

For whole exome sequencing and Sanger Sequencing genomic DNA was extracted from $CD4^+$ T cells, isolated from plck-GAPDH tumors by negative microbead selection (see above), using the Nucleospin Tissue Kit (Macherey Nagel, #740901)

Whole exome sequencing

Genomic DNA was extracted from $CD4^+$ T cells as mentioned above. Paired-end DNA library was prepared according to the manufacturer's instructions (Agilent). The adapter-modified gDNA fragments were enriched by six cycles of PCR. Whole exome capture was carried out using Agilent's SureSelect Kit. After DNA quality evaluation, pooled samples were sequenced on Illunima Hiseq 2000.

Raw data were first filtered using an in house quality control. Paired-end clean reads are aligned to the reference genome (UCSC hg19) using Burrows–Wheeler Aligner (BWA) software(Li and Durbin, 2009). If a read or reads pair is mapped to multiple positions, BWA will choose the most likely placement. While if two or more most-likely placements are present, BWA will choose any one randomly. Aligned reads were realigned to the genome. Genome Analysis Toolkit (GATK)(DePristo et al., 2011) was used to ignore those duplicates resulted from PCR amplification with Picard-tool. We utilized the INDELrealigner and RealignerTargetCreator in GATK do realignment around the INDELS according to GATK best practice. Furthermore, we performed base quality score recalibration with GATK to avoid system bias. After realignment to genome, we identified and filtered variants (SNP, INDELs) using GATK HaplotypeCaller and variantFiltration to guarantee meaningful analysis. Variants obtained from previous steps were compared based on the dbSNP (Sherry et al., 2001) and annotated with ANNOVAR(Wang et al., 2010).

Th RhoA genomic regions of interest was amplified by PCR with flanking HTS primer pairs. PCR amplification was carried out with Phusion High-Fidelity DNAPolymerase (Thermo Fisher), according to the manufacturer's instructions. Purified DNA was amplified by PCR with primers containing sequencing adaptors. The products were gel purified and quantified using the Quant-iT PicoGreen dsDNA Assay Kit (ThermoFisher) and KAPALibraryQuantification Kit (KAPABiosystems). Samples were sequenced on an Illumina MiSeq, as previously described.

Lactate and glucose measurement

To determine glucose consumption and lactate production, $CD4^+$ T cells were isolated from the spleen of WT and plck-GAPDH mice using negative selection (see above) and were activated for 48h on NA/LA hamster anti-mouse CD3e (BD Pharmingen, # 553294) coated plates (3 μg mL^{-1}) in the presence of NA/LE Hamster anti-mouse CD28(3 μg mL^{-1}; BD Pharmingen, #553294) in RPMI/10%FCS. After pre-activation, culture medium was replaced with fresh RPMI/10%FCS medium and collected 24h later. Glucose and lactate levels were determined electro-enzymatically using the YSI 2950 Biochemistry analyser (Bioprocess systems), which normalized to the number of viable cells.

Metabolic assays

OCR and ECAR were measured with an WF96 extracellular flux analyzer (Seahorse Bioscience) following protocols recommended by the manufacturer. Freshly isolated naive or activated cells were seeded on Cell Tack (Fisher Scientific, #10317081) pre-coated XF96 microplates ($2x10^5$ cells/well). The plates were quickly centrifuged to immobilize cells. Cells were maintained in a non-buffered assay medium supplemented with 25 mM glucose (Sigma, #G6152), 1 mM sodium pyruvate (ThermoFischer, #11360088) and 2 mM L-glutamine (ThermoFischer, #25030081) for OCR measurement, or with 2 mM L-glutamine for ECAR measurement. Cells were incubated in a non-CO_2 incubator for 30 minutes before starting the measurements. Glycolysis measurements were obtained after three injections, 25 mM glucose followed by 3,75 μM oligomycin (Sigma, #O4876) that inhibits mitochondrial ATP production and shifted the energy production to glycolysis. The increased ECAR revealed the maximum glycolytic capacity of T cells. The third injection was 100 mM 2-DG (Toronto Research Chemicals, #D239000), a glucose analog that inhibits glycolysis. The OCR measurements were obtained under basal conditions and in response to mitochondrial inhibitors, 3.75 μM oligomycin, 2 μM FCCP (Sigma, #C2759) and 1 μM rotenone (Sigma, #R8875) and 2 μM antimycin A (Sigma, #A8674).

2-NBDG uptake

$2x10^5$ cells were incubated in glucose free RPMI/10%FCS/1%Penicilin/streptamidin medium containing 100 μM 2-NBDG (Fischer Scientific, #N13195) for 2 hours before measuring fluorescence by flow cytometry.

IgG determination in mouse serum

IgG isotyping for IgG_1, IgG_{2a}, IgG_{2b}, IgG3, IgA, IgM, Kappa light chain or lambda chain was performed using the Pierce Rapid ELISA Mouse mAb Isotyping Kit from Invitrogen/Thermofisher Scientific (#37503) according to manufacturers' instructions. Sera were diluted 1/15 into TBS buffer provided in the kit.

Measurement of GAPDH activity

Splenocytes from treated and vehicle mice were lysed in buffer A (10 mmol/L HEPES (pH 7.4), 150 mmol/L NaCl, 5 mmol/L EDTA, 1% NP40, 10 µg mL^{-1} aprotinin, 1 mmol/L phenylmethylsulfonyl fluoride and 10 µmol/L leupeptin). 10 µg of proteins were incubated in GAPDH activity buffer (0.25 mmol/L NAD (Sigma, #N1636), 3.3 mmol/L DTT, 13 mmol/L $Na_4P_2O_7$ (Sigma, #S9515) (pH 8.5), 26 mmol L^{-1} sodium arsenate (Sigma, #A6756), and 25 mmol/L D-glyceraldehyde-3-phosphate (Sigma, G5376) in a black 96-well plate (Cellstar). GAPDH activity was measured on a fluoroscan at 445 nm after excitation at 340 nm as the increase in fluorescence related to NADH accumulation. GAPDH activity is expressed as the delta absorbance (representing the speed of NADH production) per milligram of protein.

Cell proliferation detection

For cell cycle entry analysis 10^6 $CD4^+$ T cells were activated by anti-CD3 and anti-CD28 (see TCR signaling above) for 6h and 24h and intracellular staining was performed using the mouse anti-Ki67-PE kit (BD Pharmingen, # 556027) according to manufacturer's instructions.

CFSE staining was performed on 10^6 $CD4^+$ T cells activated by anti-CD3 and anti-CD28 for 4 days (see TCR signaling above) according to manufacturer's indications (BD Biosciences, # 565082).

Anti-nuclear antibody detection

These assays were performed using the NOVA Lite HEp-2 kit (INOVA Diagnostics, Inc.)

according to the manufacturer's directions sera were diluted at 1:50 and 1:100 in PBS. Slides were incubated with anti-mouse IgG-FITC conjugate and visualized with a Zeiss Axioplan 2i microscope. Pictures were taken with an AxioCam HRm camera (Carl Zeiss International, Thornwood, NY). Data were analyzed using AxioVision LE.

ADP-Glo experiments

Kinase inhibition assay for NIK were performed with the use of ADP-Glo™ Kinase Assay following manufacturer protocol (Promega, Charbonnières-les-Bains, France) and with the following conditions: 10nM NIK, 10 to 100nM MBP (protein substrate), 10 to 100µM ATP, incubation time was 30 min at 25°C. For each experimental condition a blank assay without enzyme was used as a control of ATP non-enzymatic hydrolysis.

Biotin conjugated drug affinity precipitation

A375 cells were grown in 150 mm dishes until they reached 50% confluence and then lysed with a 10mM phosphate buffer pH=7.5 containing 250mM NaCl, 0.2% Triton-X100. Crude extract was then centrifuged at 5000xg for 10 min to remove cell debris. 1 mL of supernatant with a protein concentration of 7 mg/mL was then incubated with 100µM of one of the following conditions: biotin, phenyl-biotin, aminoquinolinil-biotin, NIK^{inh}-biotin, NIK^{inh}-biotin and 1X excess of free drug, NIK^{inh}-biotin and 10X excess of free drug. Solution were incubated overnight at 4°C under stirring conditions and then incubated with streptavidin magnetic beads (Roche, Germany; Cat. No. 11 641 778 001) for 2 hr. At the end of the incubation beads were washed 4 times with 1 volume of lysis buffer with the use of a magnetic rack. Protein attached to the beads were eluted out by adding 100mL of Laemmli sample buffer and used for further analysis.

Comparison of NF-kB and NIK knock-down by siRNA treatment and NIK inhibitor treatment

Typically, 50000 cells (A375, C12.06, A549) were plated in six-well culture plates and transfected with 30 or 50 nM siRNAs using Lipofectamine RNAimax reagent (Invitrogen,

Carlsbad, CA, USA) according to the manufacturer's protocol. If not otherwise noted, the cells were incubated with the 3 different siRNAs per target for 4 days prior to harvesting for further experiments. siRNA against NF-kB2 (FlexiTube Genesolution GS4791) and against NIK (FlexiTube Genesolution GS9020) and negative control siRNA were purchased from Qiagen. Under the same conditions these cells and non tumoral cells (melanocytes and fibroblasts) were determined by FACS and normalized to the corresponding DMSO-treated control cells.

Different B cell lymphoma cell lines (u2932, Karpas 422, SU-DHL-6) were treated with NIK^{inh} (10 μM, 96hr) or vehicle (DMSO) and the cell numbers were determined. Healthy human $CD4^+$ T cells and human AITL patient biopsies were stimulated through the TCR and treated with NIK^{inh} (10 μM, 48hr) or vehicle (DMSO) and the $CD4^+$ T and B cell numbers were determined. The cell numbers were normalized to the corresponding DMSO-treated control cells.

Data and Code Availability

The [datasets/code] for RNAseq and whole exome sequencing generated during this study are available [GSE121748 /yjmnaqagjnwxrcn; www.ncbi.nlm.nih.gov/geo]

QUANTIFICATION AND STATISTICAL ANALYSIS

Statistical analysis were conducted using Microsoft excel 2013 and Prism software v6.0 (GraphPad Software, La Jolla, CA, USA). Results are indicated as means ± SD (standard deviation) in the figure legends unless otherwise. For statistical testing of significance a student's t-test or one way ANOVA was used and p values are indicated in the figure legends. A p value < 0.05 was considered to indicate statistical significance. Mice survival curves were evaluated using Log-rank test to determine significance. All flow cytometry data shown are representative of at least 3 reproduced experiments. Gene set enrichment analysis was performed as described above.

References

Ahsanuddin, A. N., Brynes, R. K., and Li, S. (2011). Peripheral blood polyclonal plasmacytosis mimicking plasma cell leukemia in patients with angioimmunoblastic T-cell lymphoma: report of 3 cases and review of the literature. Int J Clin Exp Pathol *4*, 416-420.
Alcamo, E., Hacohen, N., Schulte, L. C., Rennert, P. D., Hynes, R. O., and Baltimore, D. (2002). Requirement for the NF-kappaB family member RelA in the development of secondary lymphoid organs. J Exp Med *195*, 233-244.
Algul, H., Treiber, M., Lesina, M., Nakhai, H., Saur, D., Geisler, F., Pfeifer, A., Paxian, S., and Schmid, R. M. (2007). Pancreas-specific RelA/p65 truncation increases susceptibility of acini to inflammation-associated cell death following cerulein pancreatitis. J Clin Invest *117*, 1490-1501.
Bachmann, I. M., Halvorsen, O. J., Collett, K., Stefansson, I. M., Straume, O., Haukaas, S. A., Salvesen, H. B., Otte, A. P., and Akslen, L. A. (2006). EZH2 expression is associated with high proliferation rate and aggressive tumor subgroups in cutaneous melanoma and cancers of the endometrium, prostate, and breast. J Clin Oncol *24*, 268-273.
Balmer, M. L., Ma, E. H., Bantug, G. R., Grahlert, J., Pfister, S., Glatter, T., Jauch, A., Dimeloe, S., Slack, E., Dehio, P.*, et al.* (2016). Memory CD8(+) T Cells Require Increased Concentrations of Acetate Induced by Stress for Optimal Function. Immunity *44*, 1312-1324.
Bhat, P., Leggatt, G., Waterhouse, N., and Frazer, I. H. (2017). Interferon-gamma derived from cytotoxic lymphocytes directly enhances their motility and cytotoxicity. Cell Death Dis *8*, e2836.
Burstein, E., and Duckett, C. S. (2003). Dying for NF-kappaB? Control of cell death by transcriptional regulation of the apoptotic machinery. Curr Opin Cell Biol *15*, 732-737.
Chaffin, K. E., Beals, C. R., Wilkie, T. M., Forbush, K. A., Simon, M. I., and Perlmutter, R. M. (1990). Dissection of thymocyte signaling pathways by in vivo expression of pertussis toxin ADP-ribosyltransferase. EMBO J *9*, 3821-3829.
Chang, C. H., Curtis, J. D., Maggi, L. B., Jr., Faubert, B., Villarino, A. V., O'Sullivan, D., Huang, S. C., van der Windt, G. J., Blagih, J., Qiu, J.*, et al.* (2013). Posttranscriptional control of T cell effector function by aerobic glycolysis. Cell *153*, 1239-1251.
Chen, Z., Yang, P., Li, W., He, F., Wei, J., Zhang, T., Zhong, J., Chen, H., and Cao, J. (2018). Expression of EZH2 is associated with poor outcome in colorectal cancer. Oncol Lett *15*, 2953-2961.
Chiche, J., Pommier, S., Beneteau, M., Mondragon, L., Meynet, O., Zunino, B., Mouchotte, A., Verhoeyen, E., Guyot, M., Pages, G.*, et al.* (2015). GAPDH enhances the aggressiveness and the vascularization of non-Hodgkin's B lymphomas via NF-kappaB-dependent induction of HIF-1alpha. Leukemia *29*, 1163-1176.
Cildir, G., Low, K. C., and Tergaonkar, V. (2016). Noncanonical NF-kappaB Signaling in Health and Disease. Trends Mol Med *22*, 414-429.
Colell, A., Green, D. R., and Ricci, J. E. (2009). Novel roles for GAPDH in cell death and carcinogenesis. Cell Death Differ *16*, 1573-1581.
Colell, A., Ricci, J. E., Tait, S., Milasta, S., Maurer, U., Bouchier-Hayes, L., Fitzgerald, P., Guio-Carrion, A., Waterhouse, N. J., Li, C. W.*, et al.* (2007). GAPDH and autophagy preserve survival after apoptotic cytochrome c release in the absence of caspase activation. Cell *129*, 983-997.
Cortes, J. R., Ambesi-Impiombato, A., Couronne, L., Quinn, S. A., Kim, C. S., da Silva Almeida, A. C., West, Z., Belver, L., Martin, M. S., Scourzic, L.*, et al.* (2018). RHOA G17V Induces T Follicular Helper Cell Specification and Promotes Lymphomagenesis. Cancer Cell *33*, 259-273 e257.

Crotty, S. (2014). T follicular helper cell differentiation, function, and roles in disease. Immunity *41*, 529-542.
De Donatis, G. M., Le Pape, E., Pierron, A., Cheli, Y., Hofman, V., Hofman, P., Allegra, M., Zahaf, K., Bahadoran, P., Rocchi, S.*, et al.* (2016). NF-kB2 induces senescence bypass in melanoma via a direct transcriptional activation of EZH2. Oncogene *35*, 2735-2745.
de Leval, L., Gisselbrecht, C., and Gaulard, P. (2010). Advances in the understanding and management of angioimmunoblastic T-cell lymphoma. Br J Haematol *148*, 673-689.
de Leval, L., Rickman, D. S., Thielen, C., Reynies, A., Huang, Y. L., Delsol, G., Lamant, L., Leroy, K., Briere, J., Molina, T.*, et al.* (2007). The gene expression profile of nodal peripheral T-cell lymphoma demonstrates a molecular link between angioimmunoblastic T-cell lymphoma (AITL) and follicular helper T (TFH) cells. Blood *109*, 4952-4963.
DePristo, M. A., Banks, E., Poplin, R., Garimella, K. V., Maguire, J. R., Hartl, C., Philippakis, A. A., del Angel, G., Rivas, M. A., Hanna, M.*, et al.* (2011). A framework for variation discovery and genotyping using next-generation DNA sequencing data. Nat Genet *43*, 491-498.
Dimeloe, S., Mehling, M., Frick, C., Loeliger, J., Bantug, G. R., Sauder, U., Fischer, M., Belle, R., Develioglu, L., Tay, S.*, et al.* (2016). The Immune-Metabolic Basis of Effector Memory CD4+ T Cell Function under Hypoxic Conditions. J Immunol *196*, 106-114.
Dupuis, J., Boye, K., Martin, N., Copie-Bergman, C., Plonquet, A., Fabiani, B., Baglin, A. C., Haioun, C., Delfau-Larue, M. H., and Gaulard, P. (2006). Expression of CXCL13 by neoplastic cells in angioimmunoblastic T-cell lymphoma (AITL): a new diagnostic marker providing evidence that AITL derives from follicular helper T cells. Am J Surg Pathol *30*, 490-494.
Federico, M., Rudiger, T., Bellei, M., Nathwani, B. N., Luminari, S., Coiffier, B., Harris, N. L., Jaffe, E. S., Pileri, S. A., Savage, K. J.*, et al.* (2013). Clinicopathologic characteristics of angioimmunoblastic T-cell lymphoma: analysis of the international peripheral T-cell lymphoma project. J Clin Oncol *31*, 240-246.
Fradet, V., Lessard, L., Begin, L. R., Karakiewicz, P., Masson, A. M., and Saad, F. (2004). Nuclear factor-kappaB nuclear localization is predictive of biochemical recurrence in patients with positive margin prostate cancer. Clin Cancer Res *10*, 8460-8464.
Fu, J., Malm, I. J., Kadayakkara, D. K., Levitsky, H., Pardoll, D., and Kim, Y. J. (2014). Preclinical evidence that PD1 blockade cooperates with cancer vaccine TEGVAX to elicit regression of established tumors. Cancer Res *74*, 4042-4052.
Fujioka, S., Son, K., Onda, S., Schmidt, C., Scrabas, G. M., Okamoto, T., Fujita, T., Chiao, P. J., and Yanaga, K. (2012). Desensitization of NFkappaB for overcoming chemoresistance of pancreatic cancer cells to TNF-alpha or paclitaxel. Anticancer Res *32*, 4813-4821.
Galluzzi, L., Kepp, O., Vander Heiden, M. G., and Kroemer, G. (2013). Metabolic targets for cancer therapy. Nat Rev Drug Discov *12*, 829-846.
Gao, X., Wang, X., Pham, T. H., Feuerbacher, L. A., Lubos, M. L., Huang, M., Olsen, R., Mushegian, A., Slawson, C., and Hardwidge, P. R. (2013). NleB, a bacterial effector with glycosyltransferase activity, targets GAPDH function to inhibit NF-kappaB activation. Cell Host Microbe *13*, 87-99.
Gardam, S., Sierro, F., Basten, A., Mackay, F., and Brink, R. (2008). TRAF2 and TRAF3 signal adapters act cooperatively to control the maturation and survival signals delivered to B cells by the BAFF receptor. Immunity *28*, 391-401.
Gaulard, P., and de Leval, L. (2014). The microenvironment in T-cell lymphomas: emerging themes. Semin Cancer Biol *24*, 49-60.

Gerondakis, S., Fulford, T. S., Messina, N. L., and Grumont, R. J. (2014). NF-kappaB control of T cell development. Nat Immunol *15*, 15-25.
Grinberg-Bleyer, Y., Oh, H., Desrichard, A., Bhatt, D. M., Caron, R., Chan, T. A., Schmid, R. M., Klein, U., Hayden, M. S., and Ghosh, S. (2017). NF-kappaB c-Rel Is Crucial for the Regulatory T Cell Immune Checkpoint in Cancer. Cell *170*, 1096-1108 e1013.
Grogg, K. L., Attygalle, A. D., Macon, W. R., Remstein, E. D., Kurtin, P. J., and Dogan, A. (2006). Expression of CXCL13, a chemokine highly upregulated in germinal center T-helper cells, distinguishes angioimmunoblastic T-cell lymphoma from peripheral T-cell lymphoma, unspecified. Mod Pathol *19*, 1101-1107.
Guo, Z., Wang, H., Meng, F., Li, J., and Zhang, S. (2015). Combined Trabectedin and anti-PD1 antibody produces a synergistic antitumor effect in a murine model of ovarian cancer. J Transl Med *13*, 247.
Heissmeyer, V., and Vogel, K. U. (2013). Molecular control of Tfh-cell differentiation by Roquin family proteins. Immunol Rev *253*, 273-289.
Hoesel, B., and Schmid, J. A. (2013). The complexity of NF-kappaB signaling in inflammation and cancer. Mol Cancer *12*, 86.
Hu, H., Wu, X., Jin, W., Chang, M., Cheng, X., and Sun, S. C. (2011). Noncanonical NF-kappaB regulates inducible costimulator (ICOS) ligand expression and T follicular helper cell development. Proc Natl Acad Sci U S A *108*, 12827-12832.
Imbert, V., and Peyron, J. F. (2017). NF-kappaB in Hematological Malignancies. Biomedicines *5*.
Iqbal, J., Wright, G., Wang, C., Rosenwald, A., Gascoyne, R. D., Weisenburger, D. D., Greiner, T. C., Smith, L., Guo, S., Wilcox, R. A.*, et al.* (2014). Gene expression signatures delineate biological and prognostic subgroups in peripheral T-cell lymphoma. Blood *123*, 2915-2923.
Jacquin, M. A., Chiche, J., Zunino, B., Beneteau, M., Meynet, O., Pradelli, L. A., Marchetti, S., Cornille, A., Carles, M., and Ricci, J. E. (2013). GAPDH binds to active Akt, leading to Bcl-xL increase and escape from caspase-independent cell death. Cell Death Differ *20*, 1043-1054.
Jain, S., Chen, J., Nicolae, A., Wang, H., Shin, D. M., Adkins, E. B., Sproule, T. J., Leeth, C. M., Sakai, T., Kovalchuk, A. L.*, et al.* (2015). IL-21-driven neoplasms in SJL mice mimic some key features of human angioimmunoblastic T-cell lymphoma. Am J Pathol *185*, 3102-3114.
Jimi, E., Strickland, I., Voll, R. E., Long, M., and Ghosh, S. (2008). Differential role of the transcription factor NF-kappaB in selection and survival of CD4+ and CD8+ thymocytes. Immunity *29*, 523-537.
Johnston, R. J., Poholek, A. C., DiToro, D., Yusuf, I., Eto, D., Barnett, B., Dent, A. L., Craft, J., and Crotty, S. (2009). Bcl6 and Blimp-1 are reciprocal and antagonistic regulators of T follicular helper cell differentiation. Science *325*, 1006-1010.
Kakiuchi, M., Nishizawa, T., Ueda, H., Gotoh, K., Tanaka, A., Hayashi, A., Yamamoto, S., Tatsuno, K., Katoh, H., Watanabe, Y.*, et al.* (2014). Recurrent gain-of-function mutations of RHOA in diffuse-type gastric carcinoma. Nat Genet *46*, 583-587.
Karakashev, S., Zhu, H., Wu, S., Yokoyama, Y., Bitler, B. G., Park, P. H., Lee, J. H., Kossenkov, A. V., Gaonkar, K. S., Yan, H.*, et al.* (2018). CARM1-expressing ovarian cancer depends on the histone methyltransferase EZH2 activity. Nat Commun *9*, 631.
Karin, M., Cao, Y., Greten, F. R., and Li, Z. W. (2002). NF-kappaB in cancer: from innocent bystander to major culprit. Nat Rev Cancer *2*, 301-310.

Kleffel, S., Posch, C., Barthel, S. R., Mueller, H., Schlapbach, C., Guenova, E., Elco, C. P., Lee, N., Juneja, V. R., Zhan, Q.*, et al.* (2015). Melanoma Cell-Intrinsic PD-1 Receptor Functions Promote Tumor Growth. Cell *162*, 1242-1256.
Kroemer, G., and Pouyssegur, J. (2008). Tumor cell metabolism: cancer's Achilles' heel. Cancer Cell *13*, 472-482.
Lavallard, V. J., Pradelli, L. A., Paul, A., Beneteau, M., Jacquel, A., Auberger, P., and Ricci, J. E. (2009). Modulation of caspase-independent cell death leads to resensitization of imatinib mesylate-resistant cells. Cancer Res *69*, 3013-3020.
Li, B., and Dewey, C. N. (2011). RSEM: accurate transcript quantification from RNA-Seq data with or without a reference genome. BMC Bioinformatics *12*, 323.
Li, H., and Durbin, R. (2009). Fast and accurate short read alignment with Burrows-Wheeler transform. Bioinformatics *25*, 1754-1760.
Liberti, M. V., Dai, Z., Wardell, S. E., Baccile, J. A., Liu, X., Gao, X., Baldi, R., Mehrmohamadi, M., Johnson, M. O., Madhukar, N. S.*, et al.* (2017). A Predictive Model for Selective Targeting of the Warburg Effect through GAPDH Inhibition with a Natural Product. Cell Metab *26*, 648-659 e648.
Lo, J. C., Basak, S., James, E. S., Quiambo, R. S., Kinsella, M. C., Alegre, M. L., Weih, F., Franzoso, G., Hoffmann, A., and Fu, Y. X. (2006). Coordination between NF-kappaB family members p50 and p52 is essential for mediating LTbetaR signals in the development and organization of secondary lymphoid tissues. Blood *107*, 1048-1055.
Long, M., Park, S. G., Strickland, I., Hayden, M. S., and Ghosh, S. (2009). Nuclear factor-kappaB modulates regulatory T cell development by directly regulating expression of Foxp3 transcription factor. Immunity *31*, 921-931.
Lund, K., Adams, P. D., and Copland, M. (2014). EZH2 in normal and malignant hematopoiesis. Leukemia *28*, 44-49.
Madonna, G., Ullman, C. D., Gentilcore, G., Palmieri, G., and Ascierto, P. A. (2012). NF-kappaB as potential target in the treatment of melanoma. J Transl Med *10*, 53.
Morin, R. D., Johnson, N. A., Severson, T. M., Mungall, A. J., An, J., Goya, R., Paul, J. E., Boyle, M., Woolcock, B. W., Kuchenbauer, F.*, et al.* (2010). Somatic mutations altering EZH2 (Tyr641) in follicular and diffuse large B-cell lymphomas of germinal-center origin. Nat Genet *42*, 181-185.
Mourad, N., Mounier, N., Briere, J., Raffoux, E., Delmer, A., Feller, A., Meijer, C. J., Emile, J. F., Bouabdallah, R., Bosly, A.*, et al.* (2008). Clinical, biologic, and pathologic features in 157 patients with angioimmunoblastic T-cell lymphoma treated within the Groupe d'Etude des Lymphomes de l'Adulte (GELA) trials. Blood *111*, 4463-4470.
Muto, H., Sakata-Yanagimoto, M., Nagae, G., Shiozawa, Y., Miyake, Y., Yoshida, K., Enami, T., Kamada, Y., Kato, T., Uchida, K.*, et al.* (2014). Reduced TET2 function leads to T-cell lymphoma with follicular helper T-cell-like features in mice. Blood Cancer J *4*, e264.
Nagata, Y., Kontani, K., Enami, T., Kataoka, K., Ishii, R., Totoki, Y., Kataoka, T. R., Hirata, M., Aoki, K., Nakano, K.*, et al.* (2016). Variegated RHOA mutations in adult T-cell leukemia/lymphoma. Blood *127*, 596-604.
Nagoshi, H., Kuroda, J., Kobayashi, T., Maegawa, S., Chinen, Y., Kiyota, M., Nakayama, R., Mizutani, S., Shimura, Y., Yamamoto-Sugitani, M.*, et al.* (2013). Clinical manifestation of angioimmunoblastic T-cell lymphoma with exuberant plasmacytosis. Int J Hematol *98*, 366-374.
Ng, S. Y., Brown, L., Stevenson, K., deSouza, T., Aster, J. C., Louissaint, A., Jr., and Weinstock, D. M. (2018). RhoA G17V is sufficient to induce autoimmunity and promotes T-cell lymphomagenesis in mice. Blood *132*, 935-947.

Palomero, T., Couronne, L., Khiabanian, H., Kim, M. Y., Ambesi-Impiombato, A., Perez-Garcia, A., Carpenter, Z., Abate, F., Allegretta, M., Haydu, J. E.*, et al.* (2014). Recurrent mutations in epigenetic regulators, RHOA and FYN kinase in peripheral T cell lymphomas. Nat Genet *46*, 166-170.
Patnaik, M. M., Vallapureddy, R., Lasho, T. L., Hoversten, K. P., Finke, C. M., Ketterling, R., Hanson, C., Gangat, N., and Tefferi, A. (2018). EZH2 mutations in chronic myelomonocytic leukemia cluster with ASXL1 mutations and their co-occurrence is prognostically detrimental. Blood Cancer J *8*, 12.
Pearce, E. J., and Pearce, E. L. (2018). Immunometabolism in 2017: Driving immunity: all roads lead to metabolism. Nat Rev Immunol *18*, 81-82.
Postow, M. A., Callahan, M. K., and Wolchok, J. D. (2015). Immune Checkpoint Blockade in Cancer Therapy. J Clin Oncol *33*, 1974-1982.
Raaphorst, F. M., van Kemenade, F. J., Blokzijl, T., Fieret, E., Hamer, K. M., Satijn, D. P., Otte, A. P., and Meijer, C. J. (2000). Coexpression of BMI-1 and EZH2 polycomb group genes in Reed-Sternberg cells of Hodgkin's disease. Am J Pathol *157*, 709-715.
Recaldin, T., and Fear, D. J. (2016). Transcription factors regulating B cell fate in the germinal centre. Clin Exp Immunol *183*, 65-75.
Ren, X. D., and Schwartz, M. A. (2000). Determination of GTP loading on Rho. Methods Enzymol *325*, 264-272.
Revillion, F., Pawlowski, V., Hornez, L., and Peyrat, J. P. (2000). Glyceraldehyde-3-phosphate dehydrogenase gene expression in human breast cancer. Eur J Cancer *36*, 1038-1042.
Rohde, M., Richter, J., Schlesner, M., Betts, M. J., Claviez, A., Bonn, B. R., Zimmermann, M., Damm-Welk, C., Russell, R. B., Borkhardt, A.*, et al.* (2014). Recurrent RHOA mutations in pediatric Burkitt lymphoma treated according to the NHL-BFM protocols. Genes Chromosomes Cancer *53*, 911-916.
Roth, R. B., Hevezi, P., Lee, J., Willhite, D., Lechner, S. M., Foster, A. C., and Zlotnik, A. (2006). Gene expression analyses reveal molecular relationships among 20 regions of the human CNS. Neurogenetics *7*, 67-80.
Rupec, R. A., Jundt, F., Rebholz, B., Eckelt, B., Weindl, G., Herzinger, T., Flaig, M. J., Moosmann, S., Plewig, G., Dorken, B.*, et al.* (2005). Stroma-mediated dysregulation of myelopoiesis in mice lacking I kappa B alpha. Immunity *22*, 479-491.
Sakata-Yanagimoto, M., Enami, T., Yoshida, K., Shiraishi, Y., Ishii, R., Miyake, Y., Muto, H., Tsuyama, N., Sato-Otsubo, A., Okuno, Y.*, et al.* (2014). Somatic RHOA mutation in angioimmunoblastic T cell lymphoma. Nat Genet *46*, 171-175.
Sasaki, D., Imaizumi, Y., Hasegawa, H., Osaka, A., Tsukasaki, K., Choi, Y. L., Mano, H., Marquez, V. E., Hayashi, T., Yanagihara, K.*, et al.* (2011). Overexpression of Enhancer of zeste homolog 2 with trimethylation of lysine 27 on histone H3 in adult T-cell leukemia/lymphoma as a target for epigenetic therapy. Haematologica *96*, 712-719.
Shen, H. M., and Tergaonkar, V. (2009). NFkappaB signaling in carcinogenesis and as a potential molecular target for cancer therapy. Apoptosis *14*, 348-363.
Sherry, S. T., Ward, M. H., Kholodov, M., Baker, J., Phan, L., Smigielski, E. M., and Sirotkin, K. (2001). dbSNP: the NCBI database of genetic variation. Nucleic Acids Res *29*, 308-311.
Shih, V. F., Tsui, R., Caldwell, A., and Hoffmann, A. (2011). A single NFkappaB system for both canonical and non-canonical signaling. Cell Res *21*, 86-102.
Sneeringer, C. J., Scott, M. P., Kuntz, K. W., Knutson, S. K., Pollock, R. M., Richon, V. M., and Copeland, R. A. (2010). Coordinated activities of wild-type plus mutant EZH2 drive tumor-associated hypertrimethylation of lysine 27 on histone H3 (H3K27) in human B-cell lymphomas. Proc Natl Acad Sci U S A *107*, 20980-20985.

Stone, E. L., Pepper, M., Katayama, C. D., Kerdiles, Y. M., Lai, C. Y., Emslie, E., Lin, Y. C., Yang, E., Goldrath, A. W., Li, M. O*., et al.* (2015). ICOS coreceptor signaling inactivates the transcription factor FOXO1 to promote Tfh cell differentiation. Immunity *42*, 239-251.
Sudo, T., Utsunomiya, T., Mimori, K., Nagahara, H., Ogawa, K., Inoue, H., Wakiyama, S., Fujita, H., Shirouzu, K., and Mori, M. (2005). Clinicopathological significance of EZH2 mRNA expression in patients with hepatocellular carcinoma. Br J Cancer *92*, 1754-1758.
Sun, S. C. (2017). The non-canonical NF-kappaB pathway in immunity and inflammation. Nat Rev Immunol *17*, 545-558.
Topalian, S. L., Drake, C. G., and Pardoll, D. M. (2012). Targeting the PD-1/B7-H1(PD-L1) pathway to activate anti-tumor immunity. Curr Opin Immunol *24*, 207-212.
Topalian, S. L., Taube, J. M., Anders, R. A., and Pardoll, D. M. (2016). Mechanism-driven biomarkers to guide immune checkpoint blockade in cancer therapy. Nat Rev Cancer *16*, 275-287.
Traggiai, E., Chicha, L., Mazzucchelli, L., Bronz, L., Piffaretti, J. C., Lanzavecchia, A., and Manz, M. G. (2004). Development of a human adaptive immune system in cord blood cell-transplanted mice. Science *304*, 104-107.
Vallois, D., Dobay, M. P., Morin, R. D., Lemonnier, F., Missiaglia, E., Juilland, M., Iwaszkiewicz, J., Fataccioli, V., Bisig, B., Roberti, A*., et al.* (2016). Activating mutations in genes related to TCR signaling in angioimmunoblastic and other follicular helper T-cell-derived lymphomas. Blood *128*, 1490-1502.
Vasanthakumar, A., Liao, Y., Teh, P., Pascutti, M. F., Oja, A. E., Garnham, A. L., Gloury, R., Tempany, J. C., Sidwell, T., Cuadrado, E*., et al.* (2017). The TNF Receptor Superfamily-NF-kappaB Axis Is Critical to Maintain Effector Regulatory T Cells in Lymphoid and Non-lymphoid Tissues. Cell Rep *20*, 2906-2920.
Visser, H. P., Gunster, M. J., Kluin-Nelemans, H. C., Manders, E. M., Raaphorst, F. M., Meijer, C. J., Willemze, R., and Otte, A. P. (2001). The Polycomb group protein EZH2 is upregulated in proliferating, cultured human mantle cell lymphoma. Br J Haematol *112*, 950-958.
Wang, K., Li, M., and Hakonarson, H. (2010). ANNOVAR: functional annotation of genetic variants from high-throughput sequencing data. Nucleic Acids Res *38*, e164.
Weber, B. S., Ly, P. M., Irwin, J. N., Pukatzki, S., and Feldman, M. F. (2015a). A multidrug resistance plasmid contains the molecular switch for type VI secretion in Acinetobacter baumannii. Proc Natl Acad Sci U S A *112*, 9442-9447.
Weber, J. S., D'Angelo, S. P., Minor, D., Hodi, F. S., Gutzmer, R., Neyns, B., Hoeller, C., Khushalani, N. I., Miller, W. H., Jr., Lao, C. D*., et al.* (2015b). Nivolumab versus chemotherapy in patients with advanced melanoma who progressed after anti-CTLA-4 treatment (CheckMate 037): a randomised, controlled, open-label, phase 3 trial. Lancet Oncol *16*, 375-384.
Wee, Z. N., Li, Z., Lee, P. L., Lee, S. T., Lim, Y. P., and Yu, Q. (2014). EZH2-mediated inactivation of IFN-gamma-JAK-STAT1 signaling is an effective therapeutic target in MYC-driven prostate cancer. Cell Rep *8*, 204-216.
Xiao, G., Harhaj, E. W., and Sun, S. C. (2001). NF-kappaB-inducing kinase regulates the processing of NF-kappaB2 p100. Mol Cell *7*, 401-409.
Xie, P., Stunz, L. L., Larison, K. D., Yang, B., and Bishop, G. A. (2007). Tumor necrosis factor receptor-associated factor 3 is a critical regulator of B cell homeostasis in secondary lymphoid organs. Immunity *27*, 253-267.
Xing, Y., Wang, X., Jameson, S. C., and Hogquist, K. A. (2016). Late stages of T cell maturation in the thymus involve NF-kappaB and tonic type I interferon signaling. Nat Immunol *17*, 565-573.

Xu, H., Wang, X., Lackner, A. A., and Veazey, R. S. (2014). PD-1(HIGH) Follicular CD4 T Helper Cell Subsets Residing in Lymph Node Germinal Centers Correlate with B Cell Maturation and IgG Production in Rhesus Macaques. Front Immunol *5*, 85.
Xu, Y., Chaudhury, A., Zhang, M., Savoldo, B., Metelitsa, L. S., Rodgers, J., Yustein, J. T., Neilson, J. R., and Dotti, G. (2016). Glycolysis determines dichotomous regulation of T cell subsets in hypoxia. J Clin Invest *126*, 2678-2688.
Yoo, H. Y., Sung, M. K., Lee, S. H., Kim, S., Lee, H., Park, S., Kim, S. C., Lee, B., Rho, K., Lee, J. E.*, et al.* (2014). A recurrent inactivating mutation in RHOA GTPase in angioimmunoblastic T cell lymphoma. Nat Genet *46*, 371-375.
Zehir, A., Benayed, R., Shah, R. H., Syed, A., Middha, S., Kim, H. R., Srinivasan, P., Gao, J., Chakravarty, D., Devlin, S. M.*, et al.* (2017). Mutational landscape of metastatic cancer revealed from prospective clinical sequencing of 10,000 patients. Nat Med *23*, 703-713.

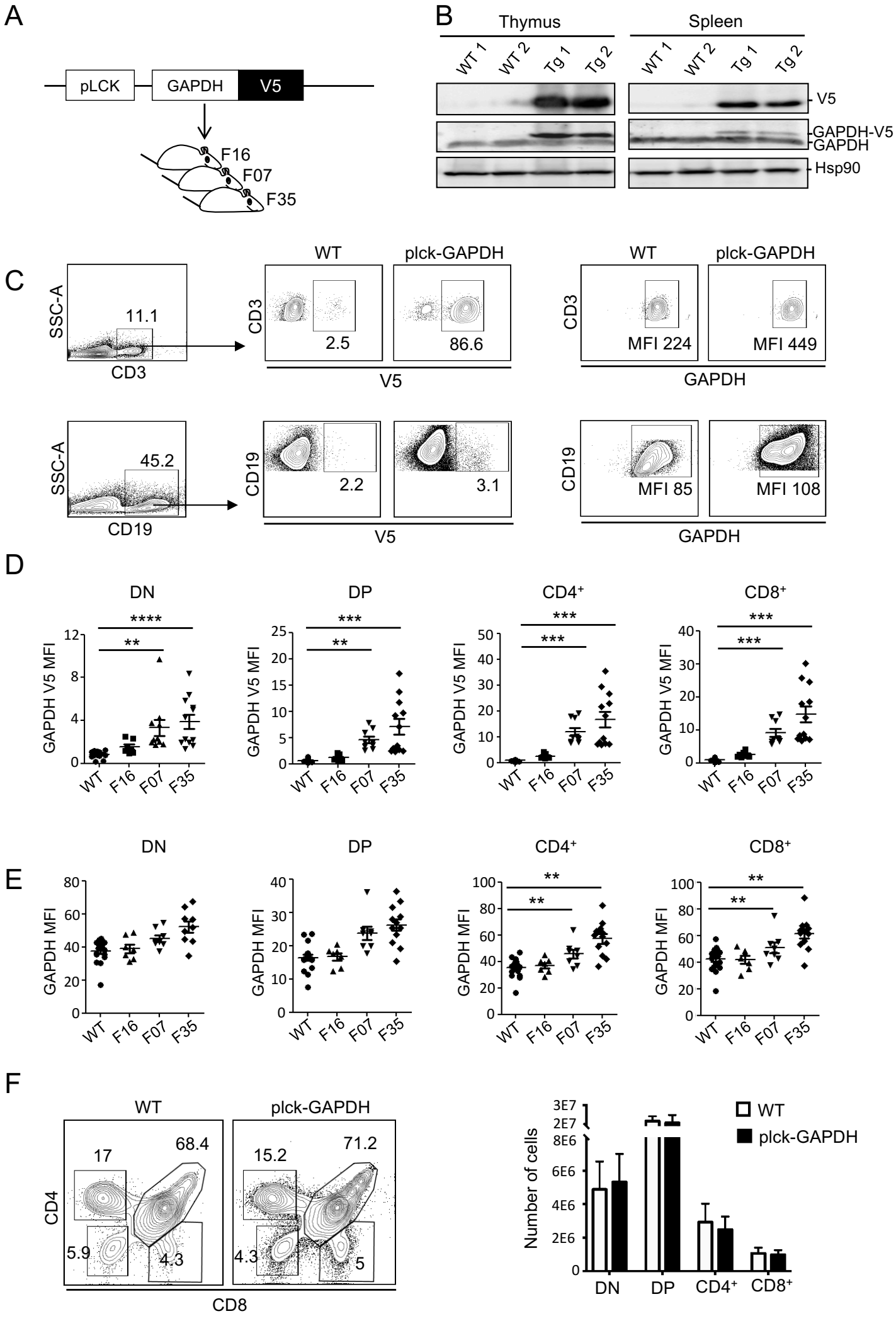
A
pLCK
GAPDH
V5
F16
F07
F35
B
Thymus
Spleen
WT 1
WT 2
Tg 1
Tg 2
V5
GAPDH-V5
GAPDH
Hsp90
C
WT
plck-GAPDH
SSC-A
11.1
CD3
2.5
86.6
V5
MFI 224
MFI 449
GAPDH
45.2
CD19
2.2
3.1
MFI 85
MFI 108
D
DN
DP
CD4+
CD8+
GAPDH V5 MFI
****
***
**
WT
F16
F07
F35
E
GAPDH MFI
F
CD4
CD8
17
68.4
5.9
4.3
15.2
71.2
4.3
5
Number of cells
DN
DP
CD4+
CD8+

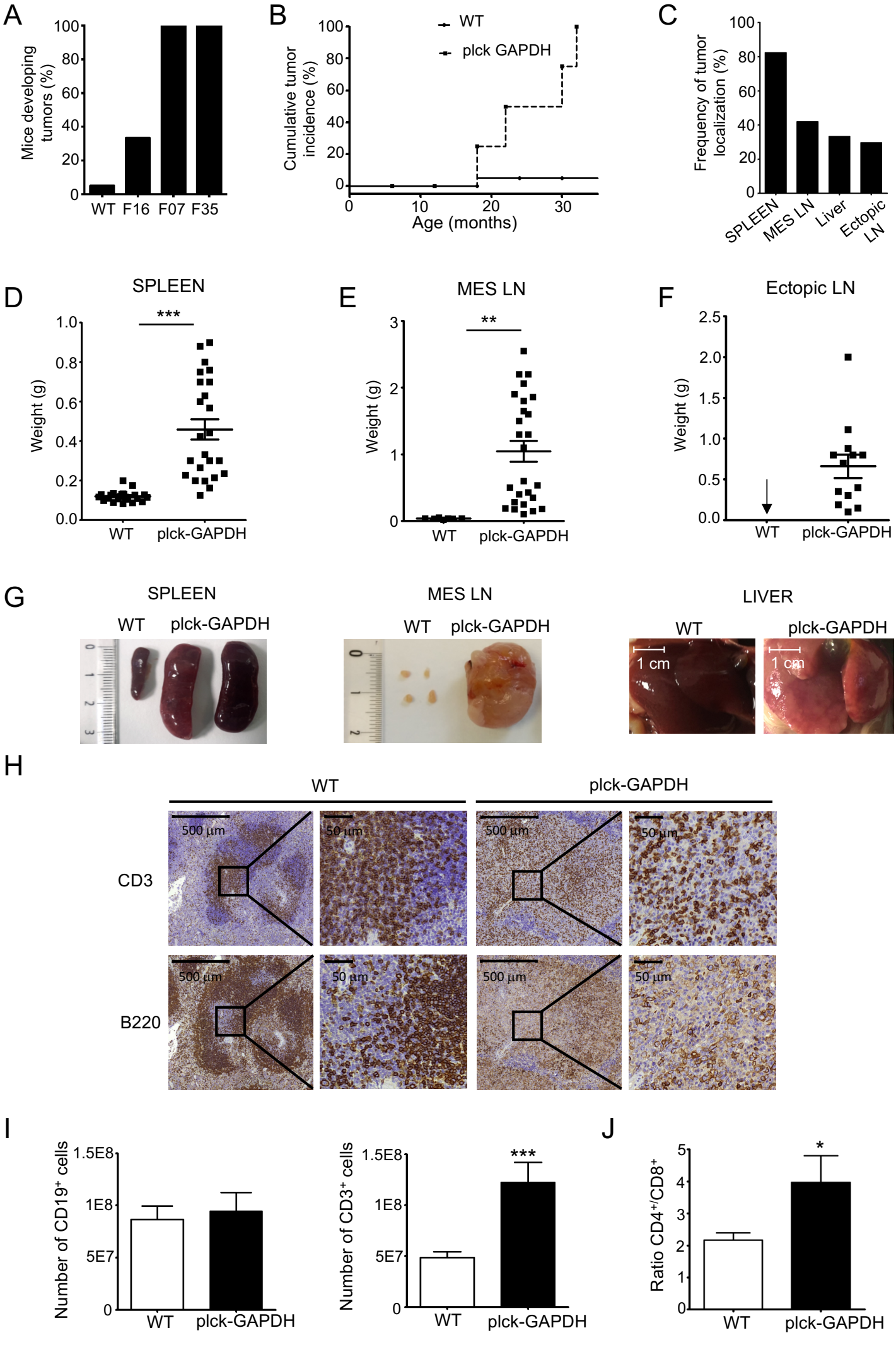
A
Mice developing tumors (%)
100
80
60
40
20
0
WT F16 F07 F35
B
Cumulative tumor incidence (%)
WT
plck GAPDH
0
10
20
30
Age (months)
C
Frequency of tumor localization (%)
SPLEEN
MES LN
Liver
Ectopic LN
D
SPLEEN
***
Weight (g)
WT
plck-GAPDH
E
MES LN
**
Weight (g)
WT
plck-GAPDH
F
Ectopic LN
Weight (g)
WT
plck-GAPDH
G
SPLEEN
WT
plck-GAPDH
MES LN
WT
plck-GAPDH
LIVER
WT
plck-GAPDH
1 cm
1 cm
H
WT
plck-GAPDH
CD3
B220
500 µm
50 µm
I
Number of CD19+ cells
1.5E8
1E8
5E7
0
WT
plck-GAPDH
Number of CD3+ cells
***
WT
plck-GAPDH
J
Ratio CD4+/CD8+
*
WT
plck-GAPDH

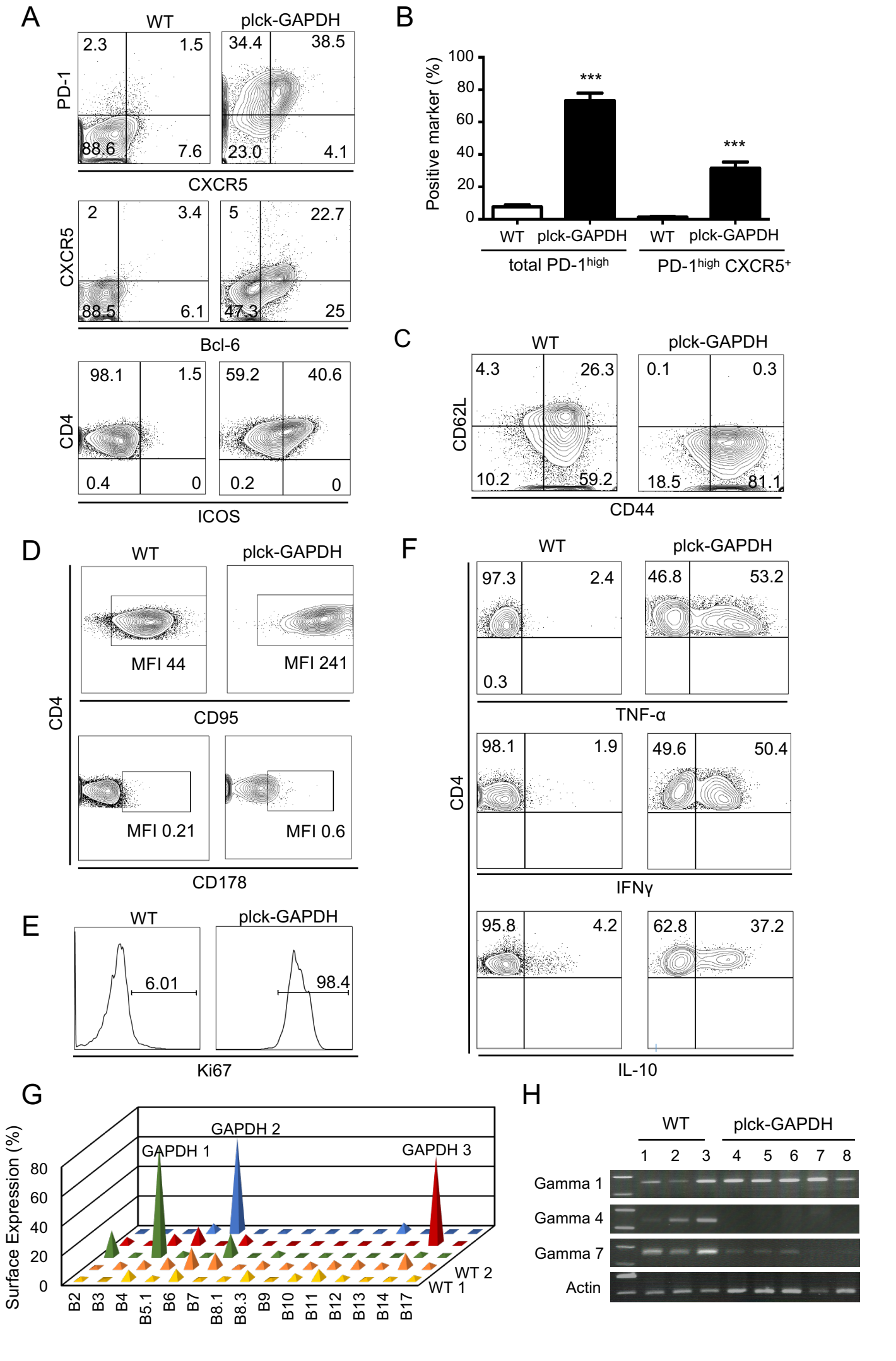
A
WT
plck-GAPDH
PD-1
2.3
1.5
88.6
7.6
34.4
38.5
23.0
4.1
CXCR5
CXCR5
2
3.4
88.5
6.1
5
22.7
47.3
25
Bcl-6
CD4
98.1
1.5
0.4
0
59.2
40.6
0.2
0
ICOS
B
Positive marker (%)
100
80
60
40
20
0
***
***
WT
plck-GAPDH
WT
plck-GAPDH
total PD-1high
PD-1high CXCR5+
C
WT
plck-GAPDH
CD62L
4.3
26.3
10.2
59.2
0.1
0.3
18.5
81.1
CD44
D
WT
plck-GAPDH
CD4
MFI 44
MFI 241
CD95
MFI 0.21
MFI 0.6
CD178
E
WT
plck-GAPDH
6.01
98.4
Ki67
F
WT
plck-GAPDH
97.3
2.4
0.3
46.8
53.2
TNF-α
CD4
98.1
1.9
49.6
50.4
IFNγ
95.8
4.2
62.8
37.2
IL-10
G
Surface Expression (%)
80
60
40
20
0
GAPDH 2
GAPDH 1
GAPDH 3
WT 2
WT 1
B2
B3
B4
B5.1
B6
B7
B8.1
B8.3
B9
B10
B11
B12
B13
B14
B17
H
WT
plck-GAPDH
1
2
3
4
5
6
7
8
Gamma 1
Gamma 4
Gamma 7
Actin

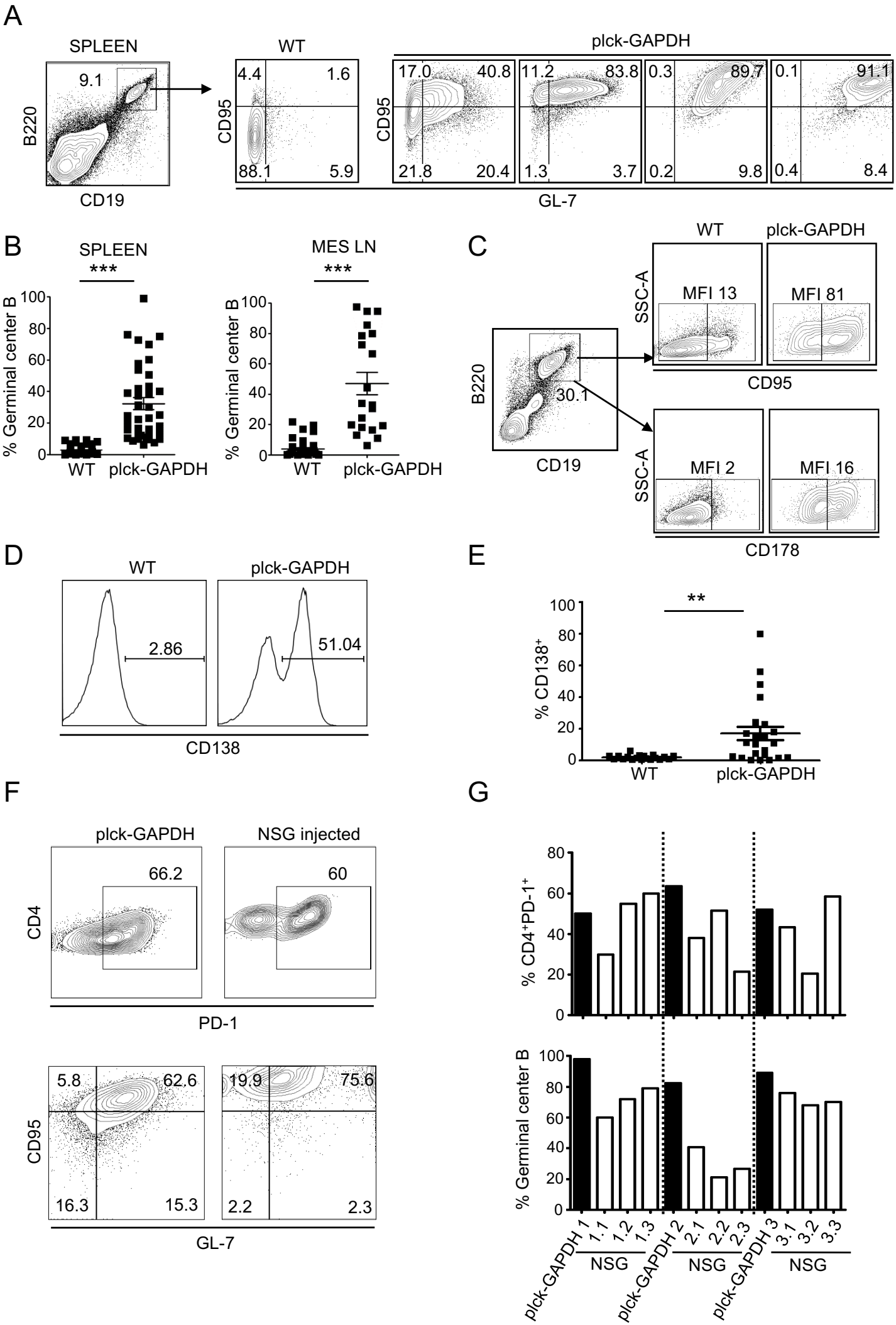
A
SPLEEN
9.1
B220
CD19
WT
4.4
1.6
88.1
5.9
CD95
plck-GAPDH
17.0
40.8
21.8
20.4
11.2
83.8
1.3
3.7
0.3
89.7
0.2
9.8
0.1
91.1
0.4
8.4
GL-7
B
SPLEEN
***
% Germinal center B
WT
plck-GAPDH
MES LN
***
C
WT
plck-GAPDH
MFI 13
MFI 81
SSC-A
CD95
B220
30.1
CD19
MFI 2
MFI 16
CD178
D
WT
plck-GAPDH
2.86
51.04
CD138
E
**
% CD138+
F
plck-GAPDH
NSG injected
66.2
60
CD4
PD-1
5.8
62.6
19.9
75.6
16.3
15.3
2.2
2.3
CD95
GL-7
G
% CD4+PD-1+
% Germinal center B
plck-GAPDH 1
1.1
1.2
1.3
NSG
plck-GAPDH 2
2.1
2.2
2.3
NSG
plck-GAPDH 3
3.1
3.2
3.3
NSG

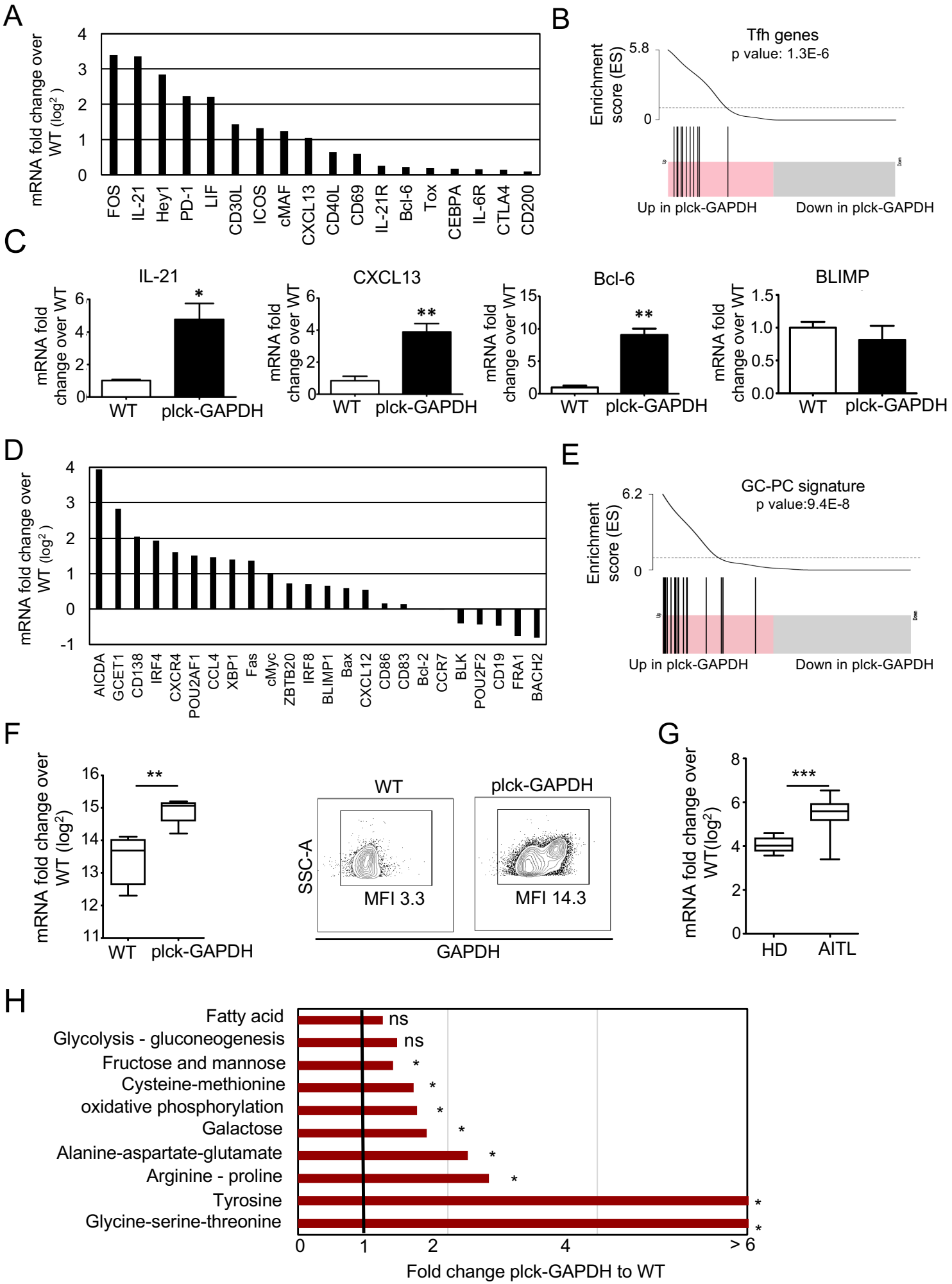
A
mRNA fold change over WT (log2)
FOS
IL-21
Hey1
PD-1
LIF
CD30L
ICOS
cMAF
CXCL13
CD40L
CD69
IL-21R
Bcl-6
Tox
CEBPA
IL-6R
CTLA4
CD200
B
Tfh genes
p value: 1.3E-6
Enrichment score (ES)
5.8
0
Up in plck-GAPDH
Down in plck-GAPDH
C
IL-21
CXCL13
Bcl-6
BLIMP
mRNA fold change over WT
WT
plck-GAPDH
D
mRNA fold change over WT (log2)
AICDA
GCET1
CD138
IRF4
CXCR4
POU2AF1
CCL4
XBP1
Fas
cMyc
ZBTB20
IRF8
BLIMP1
Bax
CXCL12
CD86
CD83
Bcl-2
CCR7
BLK
POU2F2
CD19
FRA1
BACH2
E
GC-PC signature
p value:9.4E-8
Enrichment score (ES)
6.2
0
Up in plck-GAPDH
Down in plck-GAPDH
F
mRNA fold change over WT (log2)
WT
plck-GAPDH
SSC-A
MFI 3.3
MFI 14.3
GAPDH
G
mRNA fold change over WT(log2)
HD
AITL
H
Fatty acid
Glycolysis - gluconeogenesis
Fructose and mannose
Cysteine-methionine
oxidative phosphorylation
Galactose
Alanine-aspartate-glutamate
Arginine - proline
Tyrosine
Glycine-serine-threonine
ns
Fold change plck-GAPDH to WT

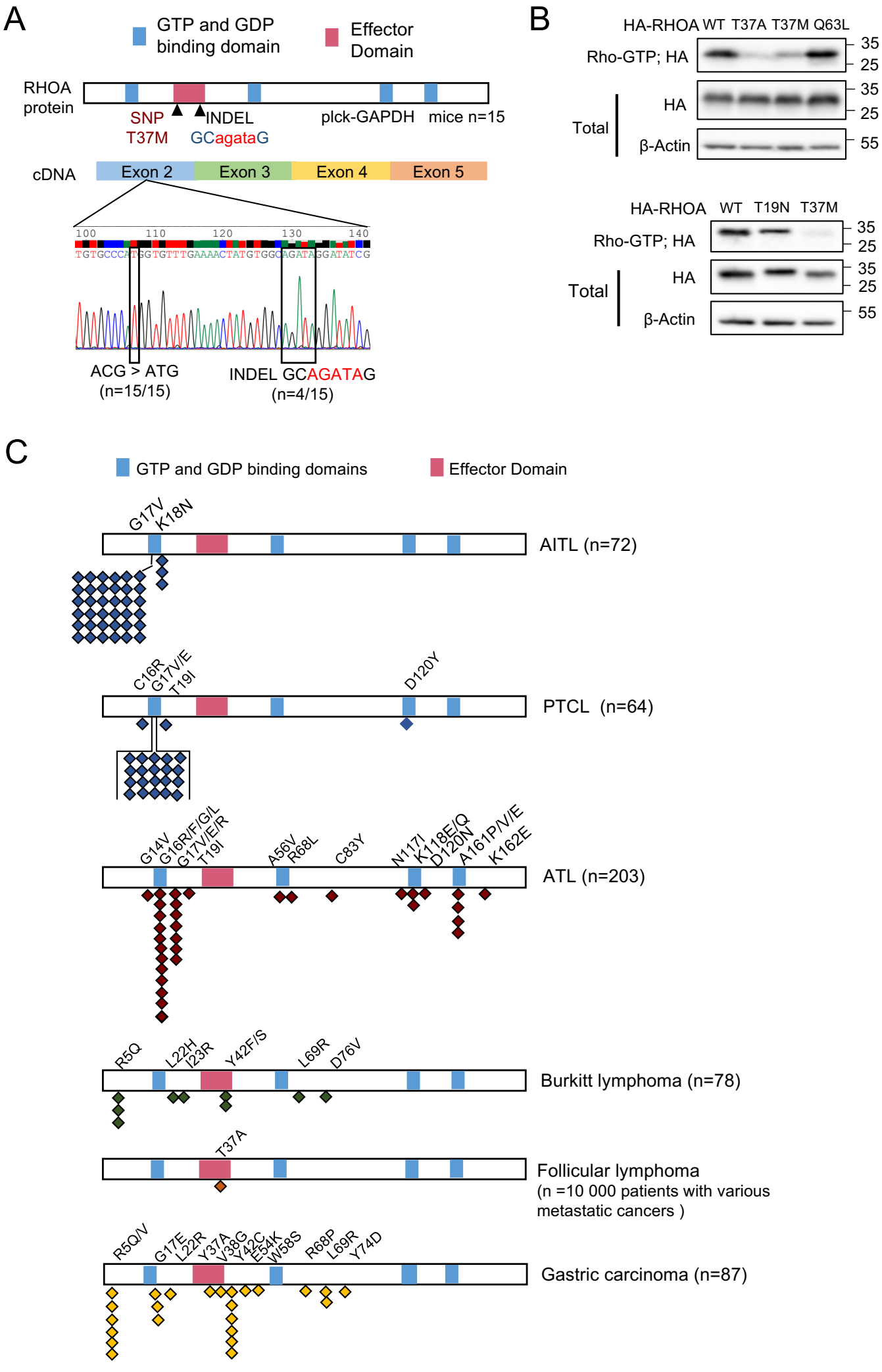
A
GTP and GDP binding domain
Effector Domain
RHOA protein
SNP T37M
INDEL GCagataG
plck-GAPDH
mice n=15
cDNA
Exon 2
Exon 3
Exon 4
Exon 5
ACG > ATG (n=15/15)
INDEL GCAGATAG (n=4/15)
B
HA-RHOA WT T37A T37M Q63L
Rho-GTP; HA
Total
HA
β-Actin
35
25
55
HA-RHOA WT T19N T37M
C
GTP and GDP binding domains
Effector Domain
G17V K18N
AITL (n=72)
C16R G17V/E T19I
D120Y
PTCL (n=64)
G14V G16R/F/G/L G17V/E/R T19I
A56V R68L
C83Y
N117I K118E/Q D120N
A161P/V/E K162E
ATL (n=203)
R5Q
L22H I23R
Y42F/S
L69R
D76V
Burkitt lymphoma (n=78)
T37A
Follicular lymphoma
(n =10 000 patients with various metastatic cancers)
R5Q/V
G17E
L22R
Y37A
V38G
Y42C
E54K
W58S
R68P
L69R
Y74D
Gastric carcinoma (n=87)

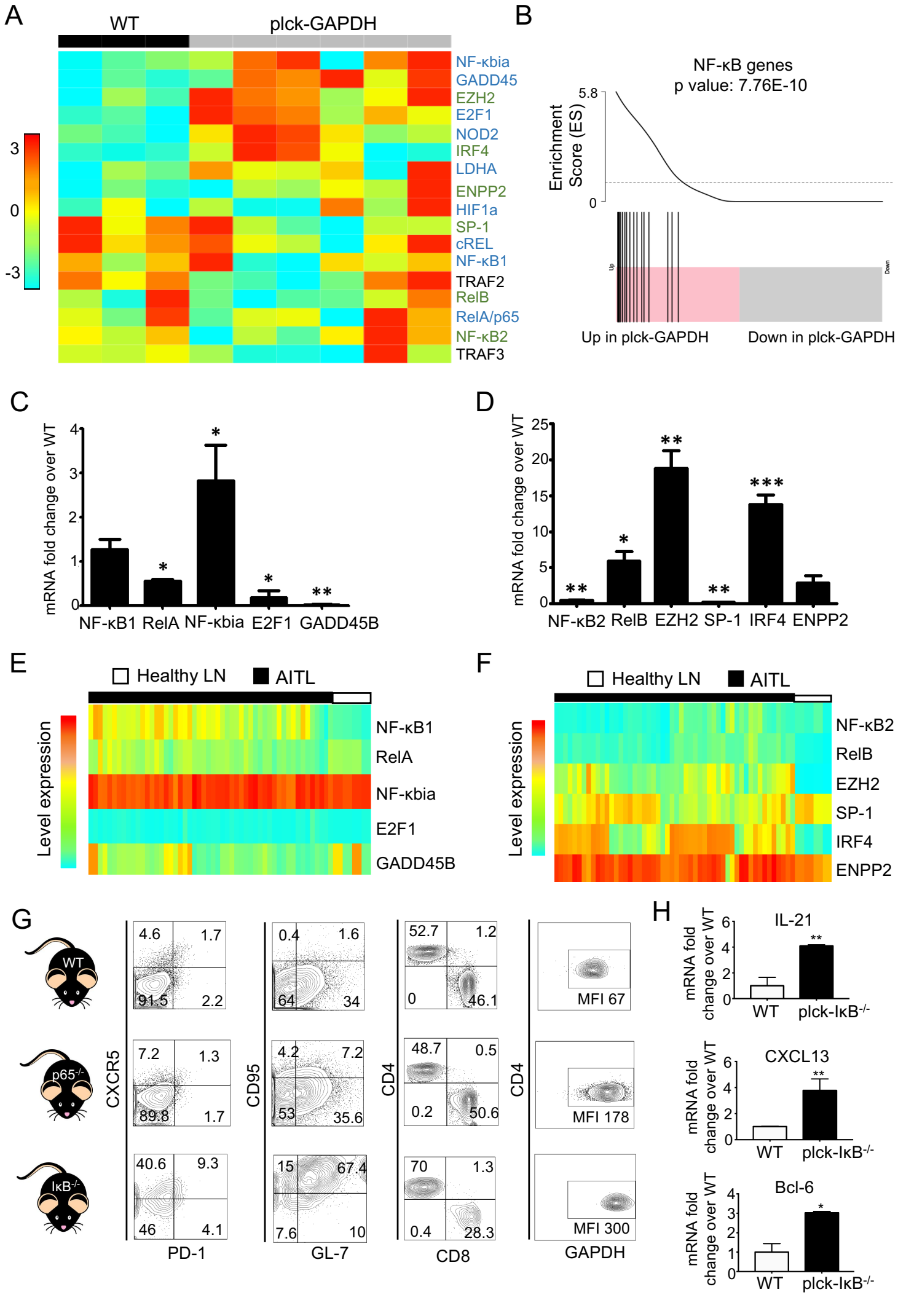
A
WT
plck-GAPDH
3
0
-3
NF-κbia
GADD45
EZH2
E2F1
NOD2
IRF4
LDHA
ENPP2
HIF1a
SP-1
cREL
NF-κB1
TRAF2
RelB
RelA/p65
NF-κB2
TRAF3
B
NF-κB genes
p value: 7.76E-10
Enrichment Score (ES)
5.8
0
Up
Down
Up in plck-GAPDH
Down in plck-GAPDH
C
mRNA fold change over WT
NF-κB1 RelA NF-κbia E2F1 GADD45B
D
mRNA fold change over WT
NF-κB2 RelB EZH2 SP-1 IRF4 ENPP2
E
Healthy LN
AITL
Level expression
NF-κB1
RelA
NF-κbia
E2F1
GADD45B
F
Healthy LN
AITL
Level expression
NF-κB2
RelB
EZH2
SP-1
IRF4
ENPP2
G
WT
p65-/-
IκB-/-
CXCR5
PD-1
4.6
1.7
91.5
2.2
7.2
1.3
89.8
1.7
40.6
9.3
46
4.1
CD95
GL-7
0.4
1.6
64
34
4.2
7.2
53
35.6
15
67.4
7.6
10
CD4
CD8
52.7
1.2
0
46.1
48.7
0.5
0.2
50.6
70
1.3
0.4
28.3
CD4
GAPDH
MFI 67
MFI 178
MFI 300
H
IL-21
CXCL13
Bcl-6
mRNA fold change over WT
WT
plck-IκB-/-

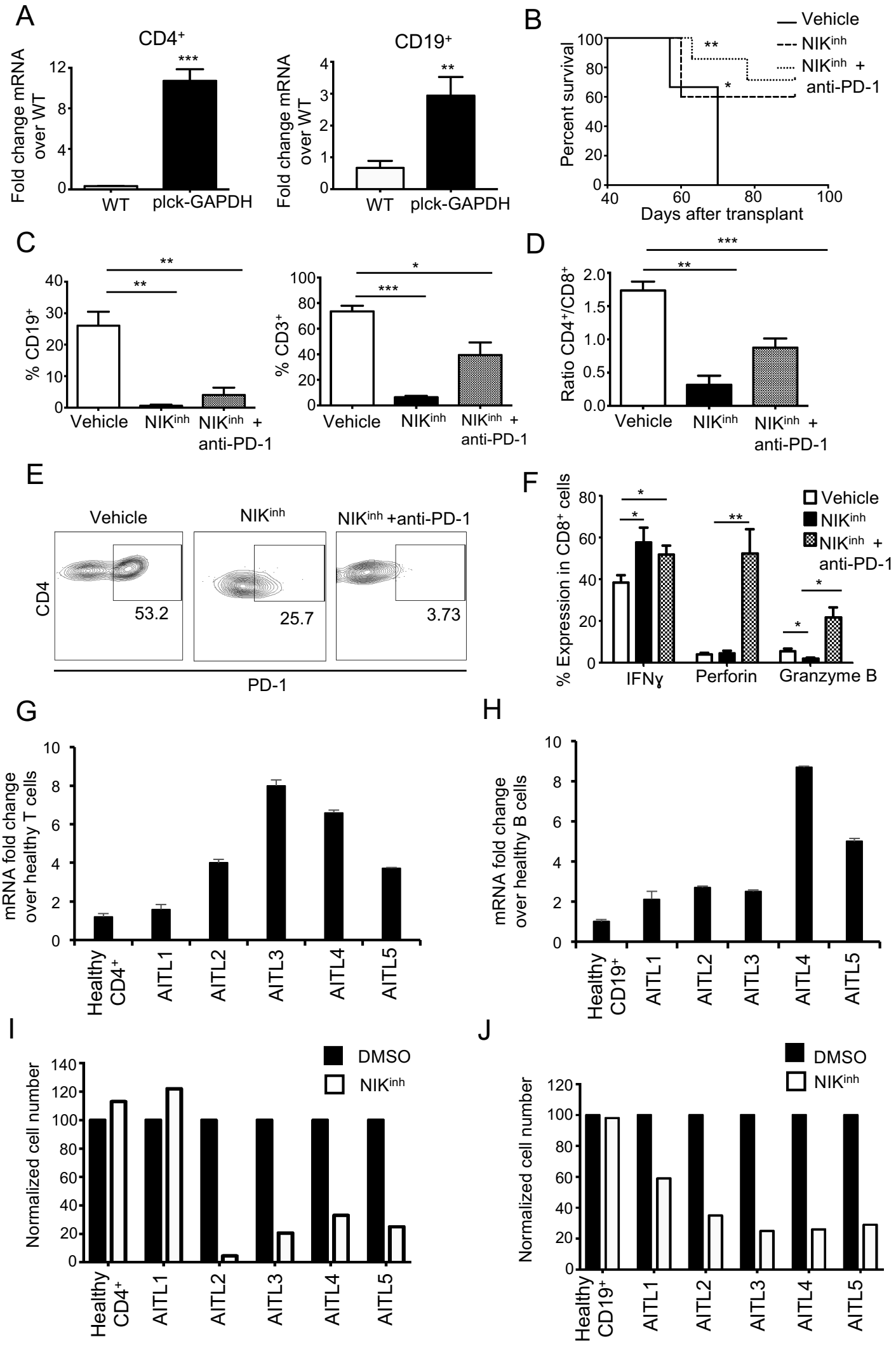
A
CD4+
CD19+
Fold change mRNA over WT
WT
plck-GAPDH
B
Vehicle
NIKinh
NIKinh + anti-PD-1
Percent survival
Days after transplant
C
% CD19+
% CD3+
Vehicle
NIKinh
NIKinh + anti-PD-1
D
Ratio CD4+/CD8+
E
Vehicle
NIKinh
NIKinh +anti-PD-1
CD4
PD-1
53.2
25.7
3.73
F
% Expression in CD8+ cells
IFNγ
Perforin
Granzyme B
G
mRNA fold change over healthy T cells
Healthy CD4+
AITL1
AITL2
AITL3
AITL4
AITL5
H
mRNA fold change over healthy B cells
Healthy CD19+
I
DMSO
NIKinh
Normalized cell number
J

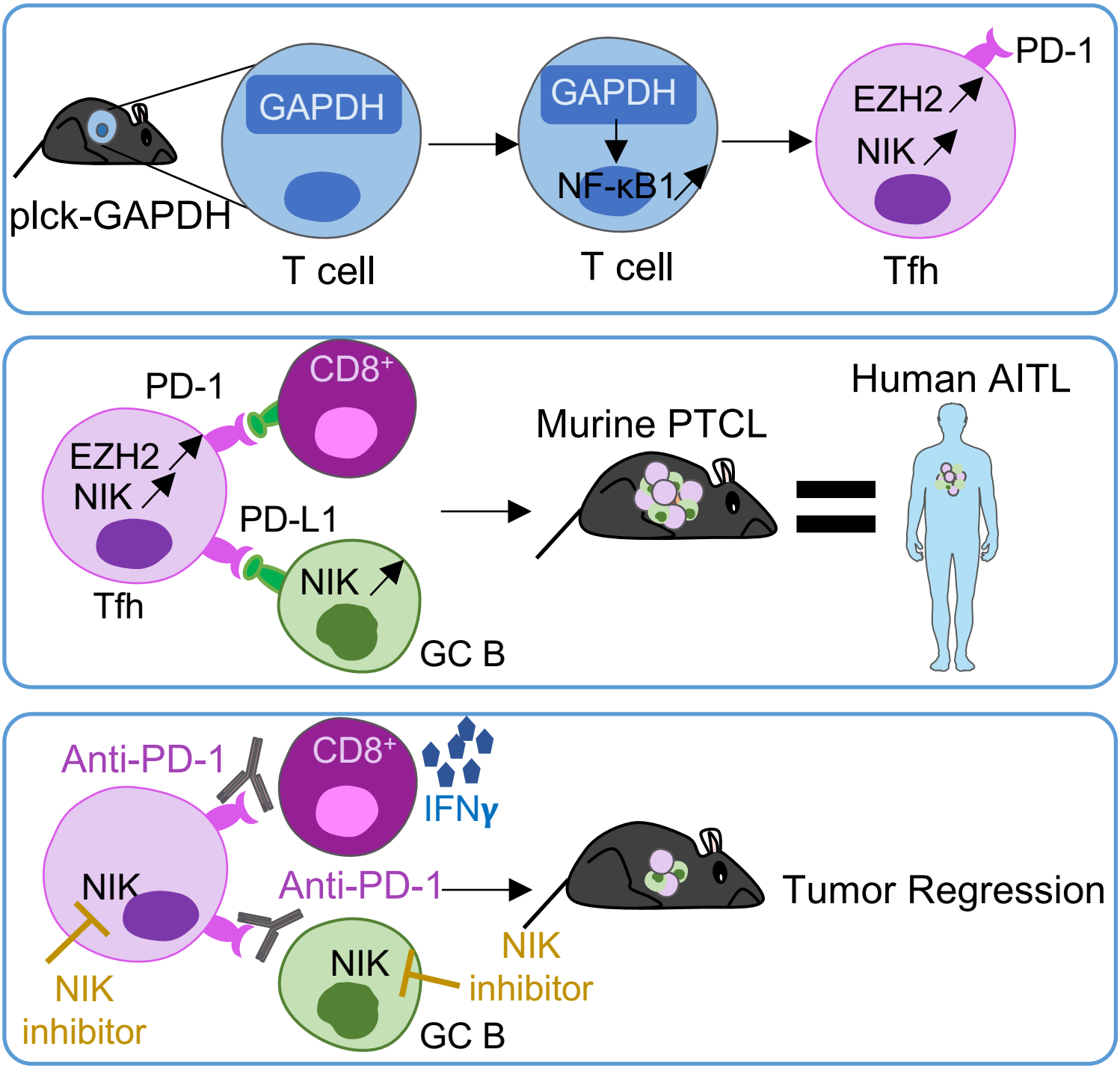
plck-GAPDH
GAPDH
T cell
GAPDH
NF-κB1
T cell
PD-1
EZH2
NIK
Tfh
PD-1
CD8+
EZH2
NIK
PD-L1
NIK
Tfh
GC B
Murine PTCL
Human AITL
Anti-PD-1
CD8+
IFNγ
NIK
Anti-PD-1
NIK
inhibitor
NIK
NIK
inhibitor
GC B
Tumor Regression